Progress in Oceanography 178 (2019) 102164

Contents lists available at ScienceDirect

Progress in Oceanography

journal homepage: www.elsevier.com/locate/pocean

Impact of swell on the wind-sea and resulting modulation of stress

Charles L. Vincent[a,*], Jim Thomson[b], Hans C. Graber[a], Clarence O. Collins III[c]

[a] Center of Southeastern Tropical Advanced Remote Sensing (CSTARS) and Department of Ocean Sciences, University of Miami, Miami, FL, United States
[b] Applied Physics Laboratory, University of Washington, Seattle, WA, United States
[c] Coastal and Hydraulics Laboratory, U.S. Army Engineering Research and Development Center, Duck, NC, United States

A B S T R A C T

Investigation of 37,106 ocean surface wave spectra from the Pacific, Atlantic Ocean, and Gulf of Mexico demonstrate that swell modulates the energy level of the high frequency tail of the wind-sea wave spectrum, altering sea surface roughness. With a mixture of sea and swell, the wind-sea part of spectra follows the well-known f^{-4} (equilibrium range) and f^{-5} (saturation range) power laws. Swell modulates the energy levels but does not change the power-law structure. For swell with minimal winds, the spectra follow the -4, -5 power-law paradigm, but energy correlates to swell steepness not wind speed. Swell shifts the transition between the two subranges towards lower frequencies. For sea-swell mixtures, a modulation factor λ is proposed that depends on wind speed and swell steepness which allows parameterization of the spectral tail. Comparison of large swell with little wind to wind-sea spectra of same height and period, indicates that there is little difference in spectral shape and suggests that the Hasselmann S_{nl} source term is likely the mechanism by which energy is transferred into the wind-sea tail causing the modulation. Analysis of 33,000+ directional spectra at Ocean Station Papa shows that the mean direction for the wind-sea high frequency tail is strongly correlated to wind direction, no matter the swell direction or steepness or level of swell dominance.

An equation for the friction velocity of a sea state with swell (u_{*s}) is developed, $u_{*s} = \lambda^{1/2} u_{*o}$ where u_{*o} is the friction velocity in the absence of swell, by neglect of the direct swell impact. Noting that this is only a partial estimate of the total measured stress, the prediction is evaluated for 3,000+ observed spectra yielding a correlation of 0.91 suggesting that it may be of consequence. Observations of u_*/u_{*o} suggest a dependence with swell steepness that is similar to that predicted by $\lambda^{1/2}$. At low winds, $\lambda^{1/2}$ overestimates the stress, but noting that it was derived absent the components from the swell frequencies. In the tail, the momentum transport is downward, while in the swell the transport is predominantly upward, suggests a possible correction for $\lambda^{1/2}$. The case of a swell generated wind is discussed.

1. Introduction

The ocean surface is a combination of waves coupled to the local wind (sea) or generated elsewhere and moving faster than the wind (swell). Statistical analysis of satellite data (Chen et al., 2002) and reanalysis wave hindcasts (Hanley et al., 2010 and Semedo et al., 2011) indicate that swell energy is dominant at least 70% of the time in the mid and higher latitudes and as much as 95% of the time in the tropics. Development of the wind-sea spectrum has received more attention than swell (e.g. Hasselmann, 1962, Hasselman et al., 1973, WAMDI Group, 1988, Tolman and Chalnikov, 1996, Ardhuin et al., 2012, Tolman et al., 2014 among others). This is logical, since swell is but the evolution of decaying wind-sea waves. Research on swell focusses on its dissipation over long distances (e.g. Snodgrass et al., 1966, Ardhuin et al., 2009, and Young et al., 2013 among others) and interaction with shorter waves (e.g. Hasselmann, 1963, Ardhuin et al., 2010 among others) or on its potential impact on the atmospheric drag (e.g. Harris, 1966; Donelan et al., 1997; Smedman et al., 1999; Grachev et al., 2001; Garcia-Nava et al., 2009, 2012; Pan et al., 2005; Potter, 2015; Sullivan et al., 2008; Sahlee et al., 2012; Högström et al., 2015; Jiang et al., 2016, and Tamura et al., 2018, Högström et al., 2018 among others). In this paper we use a data set of more than 37,000 frequency spectra drawn from four field studies in the Pacific and Atlantic Oceans and the Gulf of Mexico (Fig. 1) to investigate the interaction of the swell spectrum with the high frequency tail of the wind-sea spectrum and then consider its potential impact on momentum transport between air and ocean.

1.1. Theoretical spectrum of wind-seas when swell is absent

The characteristics of the wind-sea spectrum are best understood. Research over the past 60 years establishes that the wind-sea spectrum has a sharp peak near f_p followed by a tail composed of two frequency power law subranges: the *equilibrium range* given by

$$\phi(f) = B_4 f^{-4} \tag{1}$$

for 1.5 f_p to f_t and the *saturation range*

$$\psi(f) = B_5 f^{-5} \tag{2}$$

for f above f_t where f_t is the transition frequency (e.g. Phillips, 1958, Toba, 1973, Kitaigordskii et al., 1975, Forristall, 1981, Donelan, 1985, Phillips, 1985, Banner, 1990, and Pushkarev et al., 2003, Long and

* Corresponding author.
E-mail addresses: cvincent@cstars.miami.edu (C.L. Vincent), jthomson@apl.washington.edu (J. Thomson), hgraber@cstars.miami.edu (H.C. Graber).

https://doi.org/10.1016/j.pocean.2019.102164
Received 23 July 2018; Received in revised form 29 June 2019; Accepted 12 August 2019
Available online 19 August 2019
0079-6611/

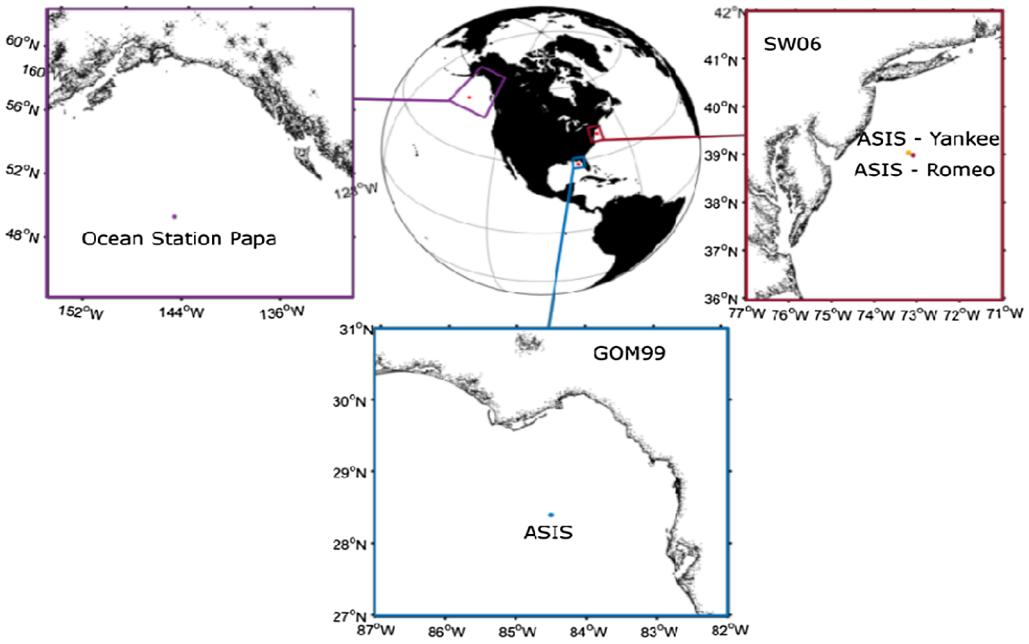

Fig. 1. Map of the buoy locations. Close ups of the coastal areas sounding each of the locations with in the Gulf of Alaska are shown in purple, within the Gulf of Mexico in blue, and within the mind-Atlantic bight in red. (For interpretation of the references to color in this figure legend, the reader is referred to the web version of this article.)

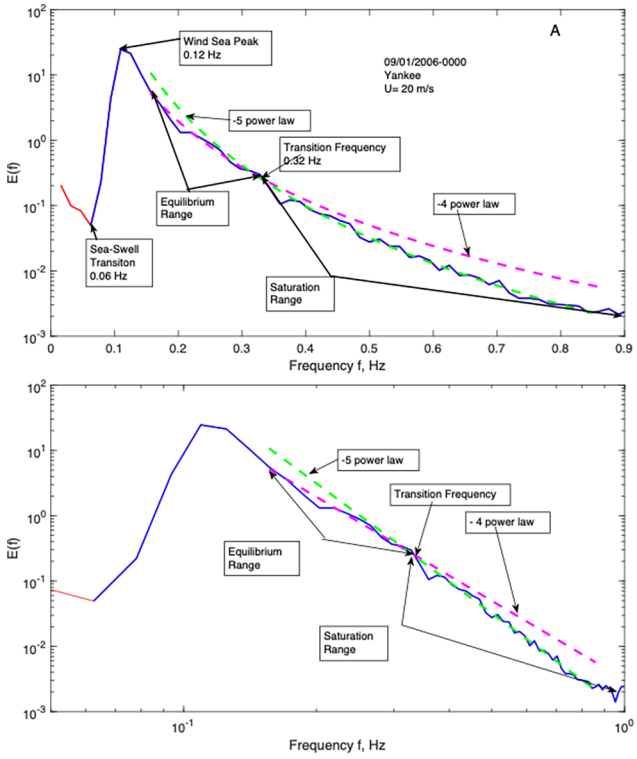

Fig. 2. Features of a wave spectrum. Top Panel is the sea spectrum (the blue line), the swell is in red. The sea-swell split frequency if $f_s = 0.08$ Hz determined by wind speed of 20 m/s. The transition frequency f_t is 0.32 Hz. Equilibrium range is from 1.5 f_{psea} to f_t, saturation range f_t to 1 Hz. Magenta curve is -4 power law constrained to fit the equilibrium range. Green curve is -5 power law constrained to fit saturation range. Date from Yankee 09/01/2006 0000 h. Lower Panel is a replot of the same spectrum in a log-log format to more clearly demonstrate the intersection of the power law curves to define the transition freqeuncy. (For interpretation of the references to color in this figure legend, the reader is referred to the web version of this article.)

Resio, 2007, Romero and Melville, 2010, and Lenain and Melville, 2017 among others). Fig. 2 provides an example of where these ranges and f_t fall on an observed wind-sea spectrum.

Kiaigorodksii et al. (1975) established that the universal scaling for these laws must lie in wave number space, k, rather than frequency which yields wave number equivalents of

$$\phi'(k) = B_4' k^{-5/2} \tag{3}$$

and

$$\psi'(k) = B_5' k^{-3} \tag{4}$$

with the primes indicating wave number spectral forms. An advantage the wave number formulation is removal of the sensitivity to surface currents that must be considered in the frequency approach. However, most observed wave spectra are frequency spectra. The research of Romero and Melville (2010) and Lenain and Melville (2017) provide an overview of the current understanding of wind-sea growth and update the fetch limited JONSWAP field experiment (Hasselmann et al., 1973) by providing observations of the wave number spectra showing the equilibrium and saturation ranges are present down to high wave numbers beyind 10 rad/m. Observations confirm that the equilibrium range coefficient (B_4) is linearly related to friction velocity as first suggested by Toba (1973) (Forristall (1981) among others); but similar dependencies have also be shown for wind speed (Miller and Vincent, 1990, Resio et al., 2004, among others). Often Monin-Obukov boundary layer theory is used to transform wind speed data into friction value estimates. Forristall (1981) indicates that B_5 can be a function of wind speed. Tamura et al. (2014) found that the saturation range is a function of wind speed until at high wind speeds and wave numbers it becomes a constant. Lenain and Melville (2017) suggest that a saturation function like B'_5 may be related to $u_*/(gH_s)^{1/2}$ where H_s is the significant wave height but it becomes constant at high wave numbers for $u_*/(gH_s)^{1/2} \sim 0.1$. Lenain and Melville (2017) following Phillips (1985) indicate that the transition from the equilibrium range to saturation range occurs at a wave number k_t

$$\frac{k_t u_*^2}{g} = 0.015 \tag{5}$$

which has a transition frequency equivalent f_t suggesting it may be related or friction velocity or wind speed. Data shown in Forristall (1981), Romero and Melville (2010) and Lenain and Melville (2017) and others note that the transition from the equilibrium to saturation range is abrupt. This suggests that at the transition $\phi'(k_t) = \psi'(k_t)$ yielding $B_5' = k_t'^{1/2} B_4'$. For a frequency spectrum the equivalent is

$B_5 = f_t B_4$.

Empirical results show that Since both the equilibrium and saturation range coefficients and f_t (or k_t) can be related to u_* (or U) below the possible fully saturated region, the full tail of the spectrum can be scaled by u_*, U or another wind speed equivalent scaling such as in Resio et al. (2004), until full-saturation occurs. It is convenient to write the entire spectral tail as

$$\Phi'(k) = [\delta\phi'(k) + (1-\delta)\psi'(k)] \quad (6)$$

with $\delta = 1$ if k is in the equilibrium range or $\delta = 0$ if k is in the saturation range. The frequency spectrum equivalent is

$$\Phi(f) = [\delta\phi(f) + (1-\delta)\psi(f)] \quad (7)$$

with $\delta = 1$ if f is in the equilibrium range or $\delta = 0$ if f is in the saturation range.

B_4 can be estimated by writing the Toba (1973) coefficient into frequency (f) space as

$$B_4 = \alpha_o U g/(2\pi)^3 \quad (8)$$

where $\alpha_o \approx 0.003$–0.005. For the transition k_t or f_t may be estimated from Eq. (5). The relation $B_5 = f_t B_4$ gives an estimate of B_5 for the frequency spectrum case. The region near the peak can be approximated from the dimensionless shape function derived for the JONSWAP spectrum. Miller and Vincent (1990) as an example show how this can be incorporated with a Toba scaling to fit observed spectra yielding both a good correlation with wind and providing provided a good estimate of γ by relating it directly to wave steepness. In summary the expected form of the wind-sea is a narrow, sharp peak spectrum about a peak wavenumber or frequency with a tail of the form given by Φ' or Φ containing appropriate k or f power laws in which both the equilibrium and saturation range coefficients are proportional to u_* or equivalently U, noting that for very high wave numbers B_5 may reach saturation. An example of a typical wind-sea spectrum is given in Fig. 2 in which the tail is not at full saturation. Almost all of the energy in the sea state is contained below the part where saturation might occur.

1.2. Motivation for research effort

The description of the wind-sea spectrum since the JONSWAP experiment has been of critical significance as the benchmark used in understanding and tuning the source-sink terms in almost all major wind wave models. But the formulation assumes zero swell in theoretical development and its validation usually involves data sets where swell is minimalized. The central question for the research presented in the paper is: Does the presence of swell alter the wind-sea spectrum, and if so, how might it influence other aspects of air-sea interaction.

As motivation for the research, we present examples from our data set, the details of which will be given in Section 2. Fig. 3 shows observed high wind-wave spectra with very low swell which conforms to the theoretical 'pure' wind-sea case. The plot contains the spectra from the Ocean Station Papa data set that are between the observed wind speeds of 20 and 22 m/s and have low swell content (less than 10% of the total energy). The spectra all have a sharp peak and tails that fall off similar to the power-law tail $\Phi(f)$ in Fig. 2. In Fig. 3 we have plotted two green lines which are the theoretical wind-sea tail (Eqs. (5), (7), (8)) based on wind speed class boundaries of U = 20 m/s and 22 m/s. If the theory is correct and the wind speeds and spectra accurate, **all** the spectral tails for the observed spectra should all fall between the two green curves. Given that there is error in wind estimates (for this data set about 1 m/s), and confidence bounds for the spectra (± 25%), we suggest that the observed spectra are consistent with the theoretical wind-sea spectrum: sharp peak, spectral tail with appropriate power-law formulation with energy levels consistent with the observed wind speeds. Whenever we examined very low swell cases in the entire data-set we found a similar result.

Fig. 4 focuses upon a wind speed range of 10–12 m/s at Ocean Papa

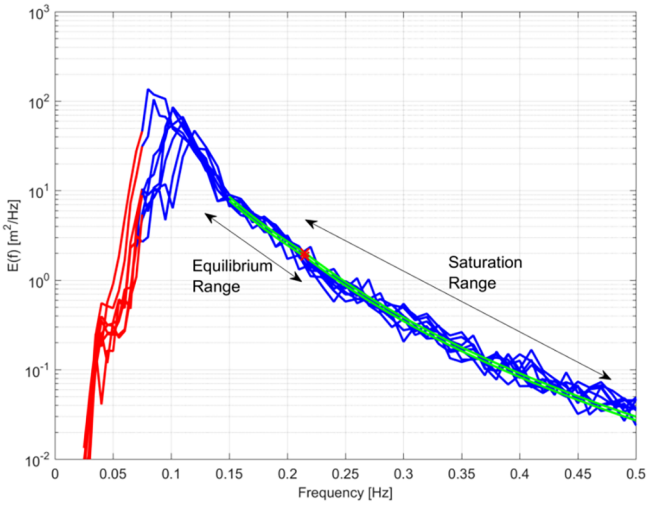

Fig. 3. Plots of the high wind speed low swell spectra from ocean station Papa. Swell frequencies are in red, wind-sea in blue. Green lines are solutions to Eq. (7) for U = 22 m/s(upper curve) and U = 20 m/s(lower curve). Red × is the transition frequency f_t. Frequency is in Hz and E(f) is m^2-s. (For interpretation of the references to color in this figure legend, the reader is referred to the web version of this article.)

where swell is largely dominant (swell energy greater than sea energy more than 85% of the time) using the same plotting convention as Fig. 3. We have provided subplots for different amounts of swell energy; 0–10%, 20–30%, 50–60%, 70–80%, 90–100% and an over-plot of all swell dominant spectra (swell energy greater than 50%) in order to show how the wind-sea spectra appear for different levels of swell energy. If there is no interaction with the swell the wind-sea portion of the spectra should look very much the same. One obvious difference is the increase in energy in the swell portion (red line) from subplots with increasing R. Our interest is in whether the wind-sea part of a spectra with swell looks like our theoretical based expectation or not. In each of the subplot there is evidence of a swarm of wind-sea tails that largely parallel the theoretical estimate for the 10 and 12 m/s tails. The case with swell energy less than 10% is equivalent to the theorical case (low swell). With increasing amounts of swell, the observed spectral tails still fall about the frequency trend of theoretical tails, but their energy levels appear more variable. If the wind-sea part of the hybrid sea-swell spectra are unaffected by swell, the observed spectral tails should fall within the green lines. There are a substantial portion that do not. Hence, the theoretical tails are a poor estimate of the actual energy levels and we conclude that the theoretical wind-sea spectrum equations for the tail do not work well when the spectrum is swell-dominant.

The lowest right hand panel (Fig. 4) provides the overall plot of all swell dominant spectra. The large number of spectra (4250) make it difficult to see how many spectral tails fall in a particular E(f) value range. For Fig. 5, we selected a frequency in the equilibrium range of 0.26 Hz and develop a histogram of the values of the observed energy level. We estimate the energy for the spectral tail from Eqs. (5), (7), and (8) for U of 10 and 12 m/s and plot them as green lines. It is clear that rather than most spectral tails falling between the green lines, a majority lie outside. We know that both the spectral estimates and winds have error. But to achieve the lowest and highest values for the tail using the theoretical equations the winds would need to be as low 5 m/s and as high as 25 m/s. Given an estimated wind speed error of 1 m/s this would be the equivalent to –6 to 14 standard deviations from the mean wind speed (11.5 m/s) which is highly unlikely. To come close the wind error estimate would need to be 4 m/s which is also unreasonable. We must conclude then that although the spectral tails follow the general trend of the theoretical tail power laws, the energy density can be significantly modulated from the expected value most

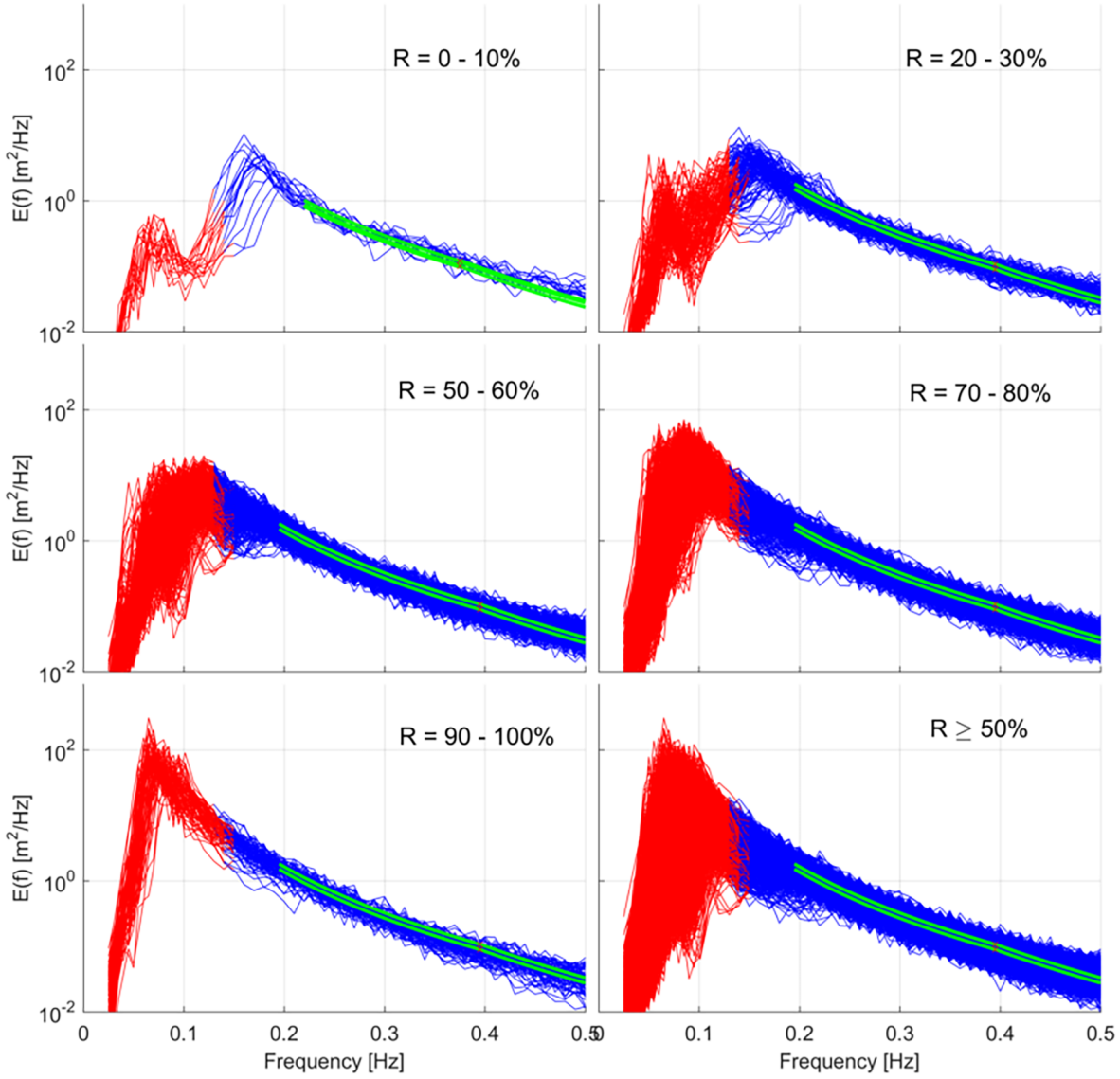

Fig. 4. Comparison of spectra for winds from 10 to 12 m/s by swell energy (R) bin. Swell component is in red, wind-sea in blue. The pair of green lines are solutions of Eq. (7) for 10 and 12 m/s. Frequency in Hz, E(f) m^2-s. (For interpretation of the references to color in this figure legend, the reader is referred to the web version of this article.)

likely due to some property of the swell.

Fig. 4 also suggest an apparent disappearance of the spectral peak when swell is dominant. Fig. 4 clearly shows distinct wind-sea peaks in the frequency range of 0.15–0.20 Hz for low swell. But as the swell energy increases, distinct wind-sea peaks become less obvious in the same frequency range (0.15–0.20 Hz). The peaks appear to shift towards the sea-swell demarcation line essentially disappearing by R > 70%. Since the number samples make distinguishing an individual tail and peak difficult, we plot the spectra with winds between 10 and 12 m/s with swell energy more than 95% of the total energy (Fig. 6). There is no obvious sharp, wind-sea peak in the frequency range (0.15–0.20 Hz). In Fig. 6 we add a fit to the largest of the wind-sea spectra in Fig. 4 over the observed swell dominant spectra. Comparison of the energy at the peak of the 'expected' wind-sea spectrum to that observes suggests that more than 80% of the wind-sea spectrum at the peak is missing. Intuitively this is the type of wind-sea spectrum we would expect if swell had no impact on the wind-sea. One can conceive that there might be residual swell energy in the wind-sea frequencies and that the wind-sea might ride above this energy. In that case, the situation is even worse because even more energy would be missing. So a significant part of the peak is missing and it looks like the wind-sea is just a continuation of the tail of the swell part of the spectrum where there are very dominant swell peaks, in this case with energy densities about 40 times the highest energy density in the wind-sea.

1.3. Key research objectives

Our paper will address two major questions that arise from these examples:

(1) Given that the swarm of wind-sea tails follow the power-law trend of Φ can this spectral tail equation be extended to fit the wind-sea tails of spectra with varying amounts of swell. If so, how do the parameters [B_4, B_5 and f_t] differ from their low swell, wind-sea counterparts.
(2) It is thought that the energy input from the wind into the higher frequencies provide a major part of the transfer of momentum from the air to waves and that this, at any frequency, is linearly related to the energy level of the wave component (Donelan et al., 2012, for example). Since it appears the presence of swell modulates the

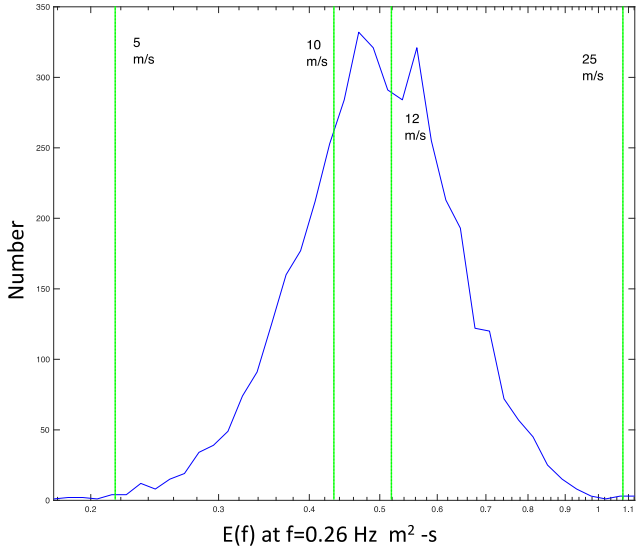

Fig. 5. Histogram of values of E(f) at f = 0.26 Hz. Winds are 10–12 m/s and percent swell energy 50–100%. Number of values (blue) plotted against the value of E(f) for f = 0.26 Hz. The values of E(f) are plotted in a log-scale to be compatible with Fig. 4. Green vertical lines are the theoretical estimates of E(f) form Eq. (7) for the given wind speeds. (For interpretation of the references to color in this figure legend, the reader is referred to the web version of this article.)

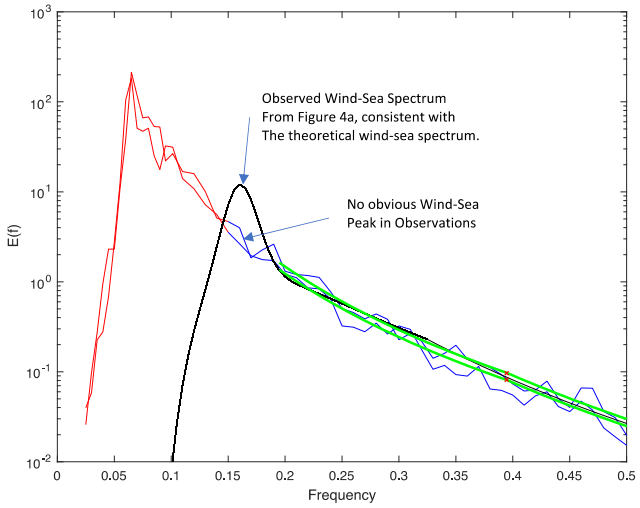

Fig. 6. Very high swell (R > 95%) spectra for winds from 10 to 12 m/s By. Swell component is in red, wind-sea in blue. Frequency in Hz, E(f) m^2-s. The pair of green lines are solutions of Eq. (7) for 10 and 12 m/s. The black line is a best fit to the highest wind-sea spectrum in Fig. 4. (For interpretation of the references to color in this figure legend, the reader is referred to the web version of this article.)

energy level of the tail, the swell can therefore in principal modulate the wind input and stress. Our second question becomes is the swell-related modulation of the wind-sea tail sufficient to alter the stress or drag.

We will not pursue the disappearance of the wind-sea peak in this paper considering that it deserves separate treatment.

1.4. Organization of the paper

The paper is organized as follows. Section 2 provides an overview of the data sources. Section 3 shows that the tails of hybrid sea-swell spectra can be expressed by an extension of the theoretical tail Φ. Section 3.1 demonstrates that Φ can be fit to almost all spectra yielding values of its parameter set [B_4, B_5 and f_t]. Section 3.2 shows how the parameter sets differ depending on swell steepness. Section 3.3 considers the case of spectra that are almost all swell and shows that these spectra can have equilibrium and saturation ranges that are a function of swell steepness not wind speed. The transition frequency is examined in Section 3.4. Section 3.5 considers issues of the wave direction for different levels of sea and swell. Section 3.6 discusses the overall conclusions of Section 3. Section 4 examines the question of whether the modulation of the energy level of the spectral tail by the swell has an impact on stress. Section 4.1 provides a discussion of relevant background information for the influence of swell on stress. Section 4.2 develops a theoretical equation for estimation of stress including the effect of modulation of the spectral tail by swell steepness. Sections 4.3 evaluates this equation and shows it explains much of the variation in stress and the need for inclusion of the effects of the momentum transfer directly from the swell. Section 4.4 considers the swell-generated wind. Section 4.5 provides a discussion of the results of Section 4. Section 5 provides a general discussion and summary of the entire paper.

2. Data sources

We examine the sea and swell interaction in deep water through analysis of a dataset of 37,106 wave spectra from the Pacific Ocean, the Gulf of Mexico, and the continental shelf of the Atlantic Ocean off New Jersey (Fig. 1) during the period 1999–2013. These data are all frequency spectra. This study requires wave spectra, wind, and atmospheric stability information. The data are drawn from three field programs: GOM99 described by Collins (2012) in the Gulf of Mexico in May 1999, the Shallow Water '06 Study (Tang et al., 2007, Collins, 2012) off the coast of New Jersey in July-September 2006, and Ocean Station PAPA in 2012–2013 (Thomson et al., 2013). We consider the spectra and wind data as accurate, trusting the efforts of the original investigators. In GOM99 and Shallow Water '06, multiple measurement systems are present allowing cross-comparisons to weed out questionable data. For the Ocean Station PAPA study, collateral data are collected during instrument redeployment cruises during October 2012. Details of each experiment relevant to our study are summarized in Table 1 and include number and types of instruments, characteristics of the wind and spectral wave products, and references to the primary study.

2.1. Wave spectrum: sea and swell partition

The dividing point between sea and swell used here is the frequency f_s

$$f_s = g/(2\pi U) \tag{9}$$

of waves moving at the speed of the wind U, or a wave age $\frac{C}{U} = 1$, where C is the celerity of waves with frequency f_s. Waves with lower frequency are classified as swell, waves of higher frequency, sea. Sometimes, the non-dimensional peak frequency of the Pierson-Moskowitz (1964) $f_{PM} = \frac{Uf_p}{g} = 0.13$ has been used. Since the spectra in this study will very often have swell, it is not always clear whether energy in the band between f_{PM} and f_s is energy transferred in via the nonlinear interactions from the sea part of the spectrum or is swell or a mixture. Likewise there may be some residual swell energy in the sea frequencies but it appears that the nonlinear interactions in a growing sea may rapidly dissipate it (Hasselmann, 1962, Tamura et al., 2009) simply note the deficiency of not using a full directional spectrum. We use Eq. (9) as the definition of f_s because it clearly delineates the spectral bands into directly coupled to the wind or not and emphasis here will be in the high frequency tail and as shown in Section 3.5 the wave direction is in the wind direction.

Table 1
Experiment information.

Wind information	Gulf of Mexico 1999	SW06 Romeo	SW06 Yankee	APL-UW PAPA
Location	200 km NW St. Petersburg FL	120 km SE Atlantic City NJ	120 km SE Atlantic City NJ	1400 km WNW Cape Flattery WA
LAT LON	28.14 N 84.5 W	39 01.1483 N 73 03.2127 W	39 04.434 N 73 09.846 W	50 N 145 W
Dates	April-May 1999	July – September 2006	July – September 2006	June 2010-October 2012
Depth	40–50 m	65–85 m	65–85	4200 m
Known Issues	Shelf edge	Close to Shore	Close to Shore	Distance Between Wind and Wave Measurements
Total Observations	1604	892	954	33,665
Wave System	ASIS buoy	ASIS buoy	ASIS buoy	Datawell buoy
Wind System	Stress capable	Stress capable	Stress capable	Wind only
Reference	Graber et al. (1999) Collins (2012)	Graber et al. (1999) Collins (2012)	Graber et al. (1999) Collins (2012)	Thompson et al. (2013)
Sensor	Gill Solent/RM Young	Gill Solent/RM Young	Gill Solent/RM Young	Gill sonic
Elevation	6.5 m	5.7 m	5.7 m	4 m adjust to 10 m neutral
Sampling Interval	20 min	20 min	20 min	Hourly
Stress Estimates	Eddy correlation	Eddy correlation	Eddy correlation	None
Air-Sea Temperature	Yes	Yes	Yes	Yes
Atmospheric Conditions	Mainly neutral	Mainly stable	Mainly stable	Neutral/mixed
Collector	RSMAS	RSMAS	RSMAS	NOAA PMEL
Sensor	ASIS wire + acceleration	ASIS wire + acceleration	ASIS wire + acceleration	Datawell acceleration
Sampling Rate	20 Hz	20 Hz	20 Hz	1.28 Hz
Number of Frequencies	64	64	64	58
Frequency Range	0–1 Hz	0–1 Hz	0–1 Hz	0–0.58 Hz
Frequencies Analyzed	0.045–0.9	0.045–0.8	0.045–0.8	0.04–0.56
Frequency Bin	0.0156	0.0156	0.0156	0.01
Directional Data Available	Yes	Limited	Limited	Yes
Comments	Deepwater for most waves	Deepwater for most waves Reduced range to minimize current effects	Deepwater for most waves Reduced range to minimize current effects	Deepwater waves
Collector	RSMAS	RSMAS	RSMAS	UW-APL

2.2. Wind observations

We will use the wind speed observed at the measurement elevation in each data set rather than correct to the reference height of 10 m. Observations (Drennan et al., 1999, Smedman et al., 1999, Drennan et al., 1993, Högström et al., 2013 among others) show that Monin-Obukov (MO) theory fails in the presence of swell hence there is no proven way for adjusting the wind profile of the atmospheric boundary layer in the presence of swell. Consequently, traditional non-dimensionalization by friction velocity or an equivalent neutral 10 m wind speed may introduce unknown errors and is not used.

Wind observations at the GOM99, Yankee and Romeo buoys are at 5.7 m above the sea surface made on the observation platform. The wind data for Papa buoy are obtained from a NOAA buoy 28 km away on the open ocean and modified into a 10-m equivalent neutral wind speed to adjust for stability. Thomson et al. (2013) evaluate the accuracy by comparisons of the NOAA buoy with measurements on site as part of short-term surveys and conclude that the wind at the NOAA buoy is consistent with the winds at the wave buoy. The NOAA buoy accuracy is 1 m/s. To gain additional perspective we correlate the winds at the NOAA buoy at hour n with winds 1 h later $(n + 1)$ over the observational period and find that the RMS error of the prediction of the winds at hour $n + 1$ from hour n is 0.85 m/s. We also compute the ratio of the wind speed at the hour difference and find that the mean ratio is near 1.0 with most of the data falling between 0.8 and 1.2. This suggests that the wind varies slowly over time and we assume that the spatial gradients are generally low. The winds at the other buoys could be correlated to synchronous observations from additional sensors nearby including a NOAA buoy. RMS differences are of order 1 m/s or less. We performed a time-lag analyses for GOM99, Yankee and Romeo buoy data such as we did for Papa and found similar error values. Our conclusion is that overall we estimate the wind speed at the measurement locations with a wind speed error of ~1 m/s.

For the Papa buoy, the raw winds are transformed to equivalent neutral winds at 10 m. For the GOM99 buoy atmospheric stability is normally neutral while at Yankee and Romeo buoys in SW06 the conditions are generally stable to strongly stable. Since Monin-Obukov theory has been shown to fail when swell is present, the impact of transforming the wind data - especially under stable conditions - is unknown. 'Un-transforming' the data at Papa likewise does not appear to be satisfactory given the uncertainties already built in from the distance between buoys. Our decision is it is best to leave each data set as it is and interpret results in terms of consistent behavior at all sites. It has the unfortunate effect however of precluding normalization by U or u_* which would allow easy combination of the four data sets into one

2.3. Spectral notation

E(f) represents the one-dimensional scalar energy spectrum as a function of frequency f. E(f) is the integral of the directional spectrum $E(f, \theta)$, where θ is angle, over all directions. In principal, the wind wave spectrum is defined to some upper frequency limit f_u here the gravity wave dispersion relation is no longer valid, although observed spectra normally have a lower frequency cut off f_c due to practical considerations. We define the following integral parameters of the spectrum:

$$\text{Total Energy } E_t = \int E(f)df \text{ over frequencies from 0 to } f_u \quad (10)$$

$$\text{Swell Energy } E_{sw} = \int E(f)df \text{ for frequencies} < f_s \quad (11)$$

$$\text{Sea Energy } E_{se} = \int E(f)df \text{ for frequencies from } f_s \text{ to } f_c \quad (12)$$

$$\text{Significant Wave Height } H_s = 4E_t^{1/2} \quad (13)$$

$$\text{Swell Wave Height } H_{sw} = 4E_{sw}^{1/2} \quad (14)$$

$$\text{Sea Height } H_{se} = 4E_{se}^{1/2} \quad (15)$$

$$\text{Mean frequency } f_M = \frac{\int fE(f)df}{E_t} \text{ over all frequencies } 0, f_c \quad (16)$$

$$\text{Mean Swell frequency } f_{sw} = \frac{\int fE(f)df}{E_{sw}} \text{ over swell frequencies} \quad (17)$$

$$\text{Mean Sea Frequency } f_{se} = \frac{\int fE(f)df}{E_{se}} \text{ over sea frequencies} \quad (18)$$

$$\text{Swell Steepness } s_{sw} = E_{sw}^{1/2} k_{sw} = E_{sw}^{1/2} (2\pi f_{sw})^2/g \quad (19)$$

$$\text{Sea Steepness } s_{se} = E_{se}^{1/2} k_{se} = E_{se}^{1/2} (2\pi f_{se})^2/g \quad (20)$$

where k_{sw} is the wave number of the mean swell frequency and k_{se} that of the mean sea frequency. We also use f_{psea} to indicate the actual peak of the wind sea. The fraction of the energy as expressed in percent in the swell band is:

$$R = \frac{E_{sw}}{E_t} x100\% \quad (21)$$

R represents relative dominance of swell versus sea. In this paper we will, unless stated otherwise, use linear wave theory so transformations between wave number and frequency are via that theory.

2.4. 'Pure' wind-sea and swell

'Pure-sea' and 'Pure-swell' are idealized concepts. For observations one way to define 'pure wind-sea' cases are those having either R < 10% and 'pure swell cases" as having R > 90%. Another definition for 'pure' wind-sea is having swell steepness $s_{sw} < 0.01$. This definition often provides examples at lower wind speeds than the R-based definition, and is physically related to wave dynamics and theory, which R is not. The steepness-based set of observations almost always include the R-defined set as a subset. It is not clear what level of swell steepness defines 'Pure Swell' while the R definition is quite clear. So, both approaches have value.

2.5. Wave and wind climate overview

Fig. 7 shows plots of sea and swell height versus wind speed for each of the four buoys. The data from the buoy at Papa has large variability due to its length of record, and open ocean location. Although the other datasets have far smaller sample sizes, the plots still show significant variability. In all plots the wind-sea height follows a near U^2 dependence with the data clustered fairly well and are near the fully developed wind-sea wave height (Resio et al., 1999, Alves et al., 2003). The only exception is for winds greater than 12 m/s at the GOM99 buoy, where some sea heights fall low. Investigation shows that these are cases where the wind rapidly spikes and then drops indicative of short duration squalls for which the wave spectrum does not have sufficient duration or fetch to achieve equilibrium. The clustering in the other plots (and for lower winds at the GOM99 buoy) suggests that the typical sea state is driven by wind fields without strong fetch limitations that change with duration slow enough to maintain a balance with wind speed. In falling winds, the sea wave height may be close to the fully developed value for the lower winds. Our results and conclusions reflect situations without strong fetch or duration limits or significant shallow water effects.

For the Papa buoy the part of the spectrum we retained from the spectral analysis only extends out to about 0.6 Hz. For the GOM99, and Romeo and Yankee buoys it extends to 0.9 Hz. This is based on analyses indicating that above these limits currents may have too much impact. Due to the different spectral limits, a bias is introduced to integral parameters derived from Papa versus the other sites.

2.6. Screening the wave spectra for study

The power law formulation (Eq. (7)) becomes a way to screen frequency spectra for study. Those spectra not following these laws are generally considered problematic most possibly effected by too large currents or instrument error. There are natural causes of non-equilibrium, such as winds that change rapidly or waves encountering current shear. When frequency spectra are used, Doppler effects from strong currents may skew the shorter waves in the spectrum away from Eq. (7).

Judging whether a spectrum has the equilibrium or saturation region involves computing the compensated spectrum $C(f, n)$ (e.g. Kitaigoroskii et al., 1975, Resio et al., 2004) for the power law f^{-n} by

$$C(f, n) = f^n E(f) \quad (22)$$

$C(f, n) = constant$ implies that the segment follows the –n power law. B_n is estimated

$$B_n = < C(f, n) > \quad (23)$$

where $< >$ is the average over the frequency range (f_1, f_2) which bounds where $C(f, n)$ is constant. This allows for a simple fit to the subrange as

$$B_n f^{-n} \quad (24)$$

For the equilibrium range, f normally begins at a frequency higher than the peak frequency of the wind-sea typically $1.5f_p$. For the saturation range f must be at frequencies higher than any in the equilibrium range. Part of the analysis is fixing the transition frequency f_t between the two ranges. If the spectra do not have the -4, -5 behavior, then the analysis will tag them for rejection.

This introduces an interesting conundrum into the study because we inherently only keep those spectra following the -4, -5 power-law paradigm. The relevant metric then should be whether we discard a significant fraction of the 37,000 spectra especially those having swell components. In Section 3.1.3 we show that we discard only about 1% of the spectra.

3. Extending the theoretical tail function $\Phi(f)$ to hybrid sea-swell spectra

One of the motivations for our research was the strong indication that the wind-sea tail of wave spectra with more than minimum swell energy appeared to follow the power-laws in the theoretical function $\Phi(f)$ but that energy levels appeared modulated above and below the theoretical 'pure' wind-sea values. In this section we describe how we fit each individual spectral tail (regardless of spectral swell content) and then investigate how the values of the three parameters [B_4, B_5 and f_t] differ from wind-seas when swell is present. 'Pure' swell is also investigated. Finally, an analysis of wind, sea and swell direction shows that even when swell is strongly dominant, the direction of waves in the tail is that of the wind.

3.1. Process for fitting the tails of mixed sea and swell spectra

In this section we show (1) the method used to fit each spectrum and (2) an evaluation of the goodness of fit. We clarify that what we consider to be the equilibrium range is the portion of the tail that is proportional to $f^{-4}$and is generally found starting somewhere near 1.5 times the wind sea peak frequency f_{psea} and ending at f_t. The saturation range is that part of the tail proportional to f^{-5} that starts where the equilibrium range ends and extends essentially to some very high frequency or wave number far beyond a wave number of 10 rad/m. The frequency in our case where the two ranges meet is f_t and part of the analysis is establishing where that will be. Fig. 2 provides an example of a single peak wind sea in which we explicitly show which parts of the tail fall under our definition. There is both thought and some evidence that at very high frequencies (or wave numbers) the tail becomes saturated, yielding a constant for the coefficient for f^{-5}, but that below this the coefficient depends on wind speed. However, we do not believe our spectra extend to sufficiently high frequencies to reach the

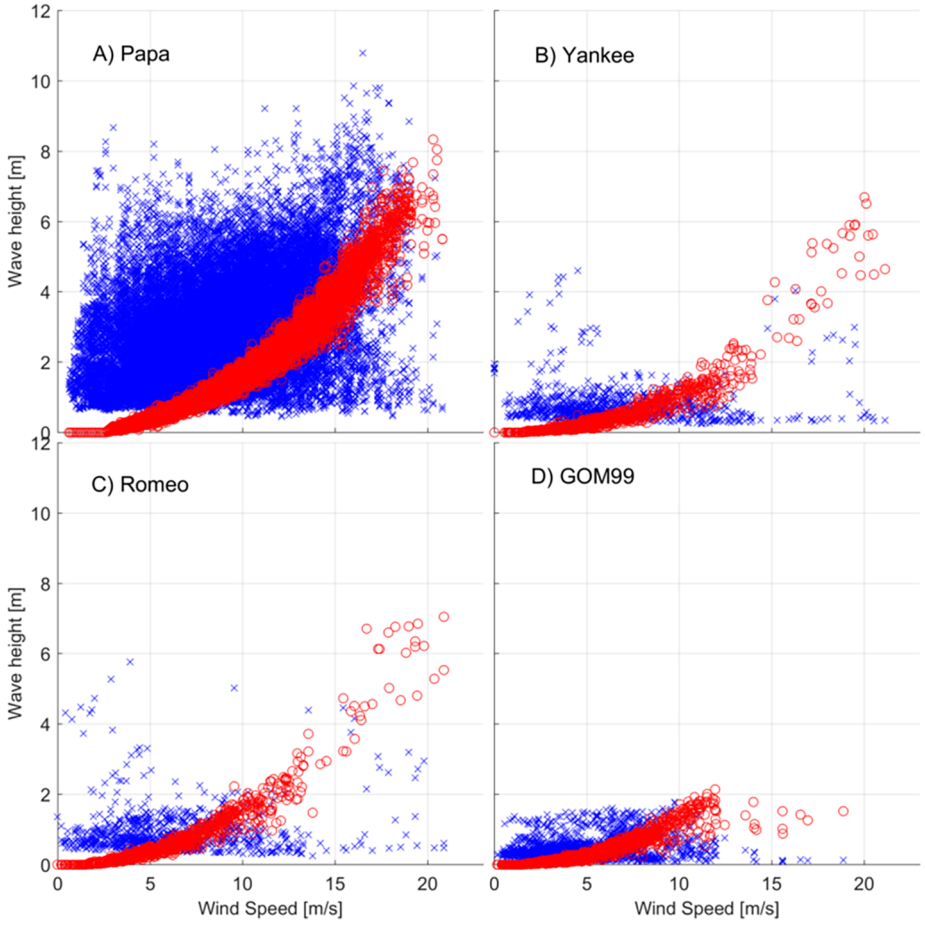

Fig. 7. Variation of sea height and swell height as a function of wind speed. The sea height (Eq. (15)) is in red and the swell height (Eq. (14)) in blue. (For interpretation of the references to color in this figure legend, the reader is referred to the web version of this article.)

anticipated full saturation.

3.1.1. Methodology

We fit each observed spectral tail to Eq. (7) to obtain $[B_4, B_5, f_t]$ and estimate a goodness of fit parameter in the following way. The compensated spectra $C(f, 4)$ is computed for the equilibrium range and $C(f, 5)$ for the saturation range). B_4 is initially estimated over the range from 1.25 the wind-sea peak frequency f_{psea} to $3.5f_{psea}$ as a first guess from $C(f, 4)$ and B_5 from $3.5f_{psea}$ to the highest observed frequency f_{max} from $C(f, 5)$. These frequency boundaries are only used to initiate the analysis; they are not the final range boundaries. We find f_t by calculating $B_5 = f_t B_4$as B_5/B_4. We then define the equilibrium range from 1.5 to f_t and the saturation range for frequencies greater than f_t.

To evaluate the goodness of fit for the $[B_4, B_5, f_t]$ we calculate a normalized, compensated tail over the frequency range considered as the tail:

$$\xi(f) = E(f)/\Phi(f) \tag{25}$$

where $E(f)$ is the observed spectra. $\Phi(f)$ is calculated from the fitted values of $[B_4, B_5, f_t]$. If the tail of the spectrum were exactly described by Eq. (7), $\xi(f)$ would equal 1 for every f in the tail, yielding $\xi_m = <\xi(f)> = 1.0$ with an in-spectrum standard deviation 0, where the subscript m indicates that the average is taken jointly over the entire equilibrium and saturation range for a spectrum. In-spectrum indicates that the standard deviation σ_ξ refers specifically to one spectral tail and measures how noisy ξ is over the individual tail. A perfect fit would be a flat line with $\xi \equiv 1$ and $\sigma_\xi \equiv 0$. So, if σ_ξ is too large it may suggest a problematic spectrum for reanalysis. We also want to know how well we did over the data set as a whole and we will compute the mean of all the ξ_m and its standard deviation. Likewise, we want to understand what the mean of the in-spectrum σ_ξ is for a full data set as well as its standard deviation. Those not fit well by our estimate $\Phi(f)$ have values of ξ_m much different from 1 and $\sigma_\xi \gg 0$. Tests where we applied $C(f, 4)$ to a range of frequencies that were actually f^{-5} yielded mean values of ξ_m for the entire tail greater than 1.5. Fits to two typical spectral tails (one a 'pure' wind-sea the other a mixed sea and swell case) are shown in Fig. 8.

3.1.2. Evaluating the goodness of fit

Data drawn from Yankee provide an example. Yankee spectra cover the frequency range up to 0.9 Hz and have high wind (22 m/s) and wave (6.5 m) conditions as well as low and a mixture of sea and swell. Fig. 9-A is a plot of the $\xi(f)$ value for every frequency for all spectra versus f/f_t (more than 22,000 values) and Fig. 9-B is a histogram of the values of ξ_m (average over the full tail) for these spectra. In Fig. 9-A each dot represents an individual value of $\xi(f)$ from each spectrum. The mean value $<\xi_m(f)>$ for the full spectral tail over all spectra is 1.0373 with a standard deviation of 0.0529 which we conclude constitutes a good fit because the mean is very close to 1 and the standard deviation is low. The average of the in-spectrum standard deviations is 0.2351 indicating that on average the perturbations about an individual ξ_m is consistent with the noise-like variability seen in typical spectra due to uncertainty in the spectral analysis. Fig. 9-A shows that in general the points lie within the band 0.7–1.3 but there are a few individual estimates that are above 2 or less than 0.5 (remembering that the points represent only 1 frequency on 1 spectrum). The analysis allows several ways to tag spectra for reanalysis- is any one value ξ suspicious or is the mean for an entire tail too large. We note that in Fig. 9-B, the values of

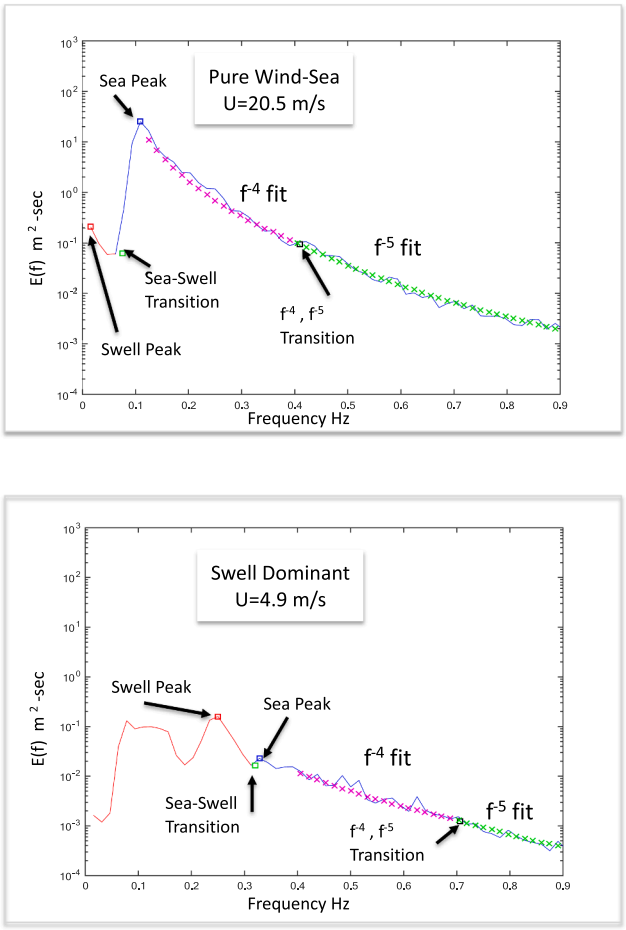

Fig. 8. Two examples of automated fits of observed spectral tails. Swell bands are in red, sea in blue. Red square shows swell peak; green square swell to sea transition; blue square wind sea peak; and the black square transition from the -4 to -5 power law. Top panel is a high wind-speed wind-sea spectrum with little swell. The bottom panel is a low wind-speed spectrum but with two swell peaks. (For interpretation of the references to color in this figure legend, the reader is referred to the web version of this article.)

ξ_m really have a fairly narrow range.

While the statistics related to the ξ_m provide a succinct summary of goodness of fit, it is also important to understand the results in terms of the spectra and the parameters. Fig. 10 provides plots of the spectral density $E(f)$ for two frequencies, one each typically in the Equilibrium Range (0.31 Hz) and the Saturation Range (0.68 Hz). The observed spectral density for a spectrum is plotted as a blue o. A green o is our estimate of that spectral density based on the value of B_4 or B_5 we estimated for that spectrum via our fitting procedure: $B_4(0.31)^{-4}$ and $B_5(0.68)^{-5}$. The most important conclusion from the plot is that observed spectral densities in both ranges increase as the wind speed increases. The semi-log-y axis was used to spread out the data points for visual examination. The red line through each curve of points is the best fit to the spectral densities against wind speed in a linear analysis. Changing the plot to the semi-log format makes the linear curve bend. The second conclusion is that our estimate of spectral density is very good, the green 'o' fall within the scatter of the blue dots and parallel its trend. Since $(0.31)^{-4}$ and $(0.68)^{-5}$ are constants, the data imply that B_5 and B_4 vary linearly with wind speed as shown in Fig. 11. The relationship between f_t and wind speed (Fig. 12) shows that the value of f_t decreases with increasing wind speeds. We can estimate k_t from f_t using linear theory and compute $u_* k_t/g$ to compare with Lenain and Melville (2017). They found $u_* k_t/g$ ranged from 0.012 to 0.025; the estimate for Yankee is 0.0203 suggesting that our estimates of f_t are consistent with other studies. In sum the fitting process appears to reconstruct the essential features of the spectral tail and in particular our fitted B_4 and B_5 reproduce the energy levels at specific frequencies in the appropriate ranges.

3.1.3. Overall results

Table 2 provides the number of spectra fit, the mean values of ξ_m over the entire set of observations and its standard deviation for the data for each of the four buoys. For clarity, ξ refers to the value of $E(f)/\Phi(f)$ for one frequency on one spectrum. ξ_m refers to the average of ξ over all the frequencies in the tail of one spectrum. Also computed is the in-spectrum standard deviation σ_ξ, which refers to the standard deviation of ξ about the mean ξ_m of one spectrum. Our objective is to have a fit of the tail which yields a value of $\xi_m = 1$ and a small variance σ_ξ^2 about it. We evaluate how well we have performed by taking the mean of ξ_m for each buoy. The mean ξ_m values ran from 1.034 to 1.056 with standard deviations of 0.06 or less. If we look at the mean values of in-spectrum standard deviations σ_ξ (over all spectra in a data set) for the 4 buoys, it ranges 0.23–0.27 with a standard deviation of 0.12 or less. We conclude that the spectral tails are well described by our equation for $\Phi(f)$ no matter the mixture of sea and swell when we have adequate frequency range for the wind conditions to expose both ranges.

At the GOM99, Romeo and Yankee buoys almost all of the spectra can be fit. But at the Papa buoy only about 15,000 can because of the 0.6 Hz cut-off. We modified the Papa analysis to use just the equilibrium range. In this case the mean ξ_m is about 1.0 with a standard deviation of 0.016 and the mean σ_ξ is 0.23 all consistent with the full spectra fits. The number that can be fit at Papa increased to 31433. For those spectra we could not fully fit, we conjecture that we would find equally good results for the entire spectrum were we able to go to 0.9 Hz given the large number that could be fit for B_4 at Papa and the good fit for the full spectrum when the spectral tail is long enough to obtain B_5 (15,000 cases).

Some spectra (2470) are rejected for analysis because the wind speed or total energy is too low and the spectra looked like noise. As a result, only 34,645 of the total number of spectra (assuming at Papa the validity for the B_4 fit would imply a full fit) are available for analysis. Of those 34,323 or 99% can be successfully fit with the statistics given in Table 2. Since swell dominant spectra are present at most buoys about 80% of the time, we conclude that we have not rejected many spectra at all by our screening requirements.

3.1.4. Discussion

These results show the spectral tails overwhelmingly follow the -4 and -5 power-law-paradigm whether the spectrum is a mixture of sea and swell or just wind-sea in three different environments using two different measurement technologies. Few spectra were excluded. Our data explicitly show that swell does not alter the frequency dependence of the wind-sea tail, a significant conclusion in itself. Still to be understood is how the relationship of [B_4, B_5 and f_t] to U differs when swell is present.

3.2. Variation of spectral parameters with wind speed

The parameters [B_4, B_5, f_t] for Φ describe our fit to a spectrum's tail. This allows specification of the energy levels of the equilibrium and saturation ranges and the location of the transition point. Section 3.1 established that these 3 factors reproduced the tail of the spectrum no matter its mixture of sea and swell for most samples in our four data sets. Below we investigate how these parameters vary when swell is present by contrasting them to 'pure' wind-sea cases.

3.2.1. Equilibrium range

Fig. 13 provides plots of B_4 versus U containing all 'pure' wind-seas cases (defined by swell steepness less than 0.015) for each of the four buoys. For all locations the $B_4 - U$ relationship is linear as expected

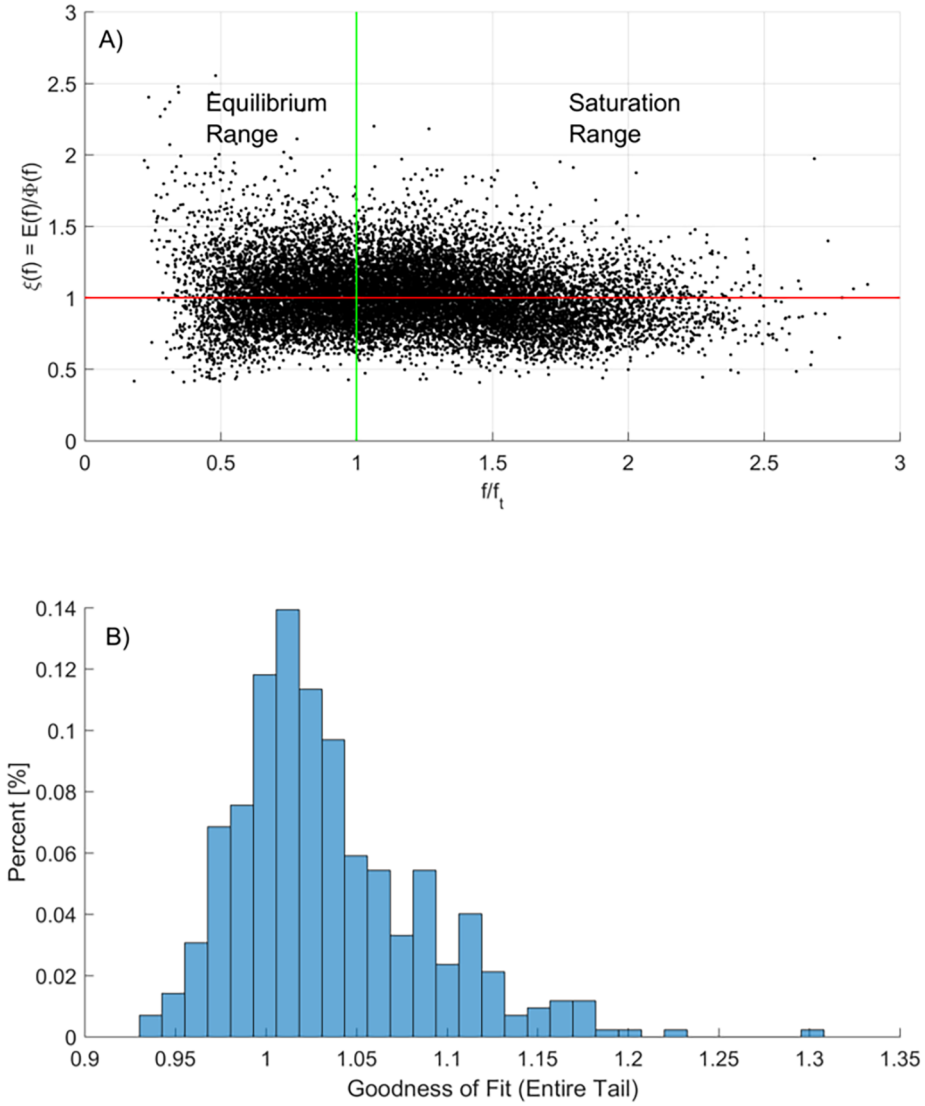

Fig. 9. Goodness of Fit for Yankee. Panel A is the value of ξ (f) = E(f)/Φ(f) for every f in the equilibrium and saturation ranges for all observed spectra plotted relative of f/f_t. Red line is the average of ξ (f) for all points. Panel B is a histogram of the values of < ξ (f) > over all f for each spectrum. (For interpretation of the references to color in this figure legend, the reader is referred to the web version of this article.)

from the literature and we conclude that our data are consistent with theory for low swell. For 'pure' wind-sea cases we will denote B_4 as B_0. The dimensions of B_4 are m^2–s^{-3}.

Fig. 14-A provides a plot of all data at Papa with each spectrum annotated by swell steepness. It is plotted semi-logarithmically to display the spread in B_4 values particularly at low wind speed. The black line drawn through the semi-log graph is the linear equation $B_0 - U$ derived for 'pure' wind-sea for each shown in Fig. 13. It appears bent because of the axis transformation. For the Papa data, the points with the lower swell steepness (0–0.02) in blue cluster about the $B_0 - U$ line. The next grouping (green) in swell steepness (0.02–0.04) is shifted higher than the blue points suggesting that on average at a given wind speed the B_4 values are higher than the lowest swell steepness cases. The next higher group, swell steepness (0.04–0.05) in magenta, lies higher than the green, the next grouping (0.05–0.06) in black lies above the magenta and the highest grouping (0.06–0.08) in red tend to lie higher than the black. This shows that at any wind speed the value of the equilibrium range coefficient tends to be larger compared to B_0 as a function of swell steepness, although there is scatter. We performed the same analysis for the other buoys showing the plots in Fig. 14b-d. The other buoys data strongly confirm the consistency of this result.

The trend is clearer in Fig. 15 where B_4 is plotted against swell steepness for specific wind speed bands for the Papa data. The trend with swell steepness is largest at 2–3 m/s, moderate at 5–6 m/s, minimal at 10–11 m/s but for 15–17 m/s the effect is essentially non-existent. We do not plot the curve for > 17 m/s because it just lies over the 15–17 m/s data. The decrease in the effect of swell with increasing wind speed is likely due to the increase in wind wave energy and its steepness. By 10 m/s the observed sea steepness significantly exceeds the swell steepness which suggests that the wind-sea swell interaction is in some sense a competition between the steepness of the swell versus that of the sea. At the mid to lower wind speeds, there is more scatter. It is possible that in these ranges the characteristics of the full spectrum such as location and number of sea and swell peaks, relative peak frequencies and swell-wind angles influence the tail of the spectrum, not just the swell steepness. This shows that swell steepness is a major factor controlling the modulation of the energy levels in the spectral tail: the larger the swell steepness the higher the B_4 and hence energy level of the equilibrium range, but the effect is wind speed dependent.

One way to display this is in terms of a factor

$$\lambda = B_4/B_0 \tag{26}$$

where B_4 is the observed value from the spectrum containing swell. B_0

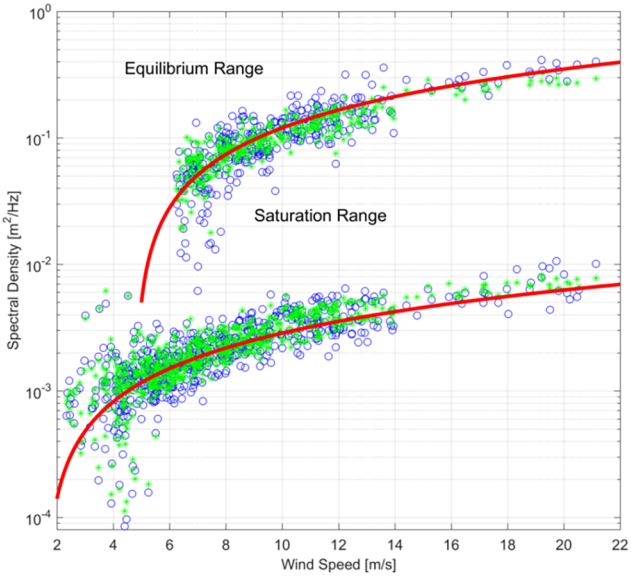

Fig. 10. Comparison of spectra energy densities for different wind speeds. Upper curve presents the values observed (blue o) of E(f) at a frequency of 0.31 Hz in the equilibrium range for each spectrum along with an estimate (green o) $B_4(0.31)^{-4}$ based on the value of B_4 fitted to that spectrum. The red line is the linear relation between the observed values at 0.31 Hz and wind speed found by a linear plot of E(f = 0.31 Hz) against U. The lower curve is a similar plot for f = 0.68 Hz. In the saturation range with the observed spectral density as a blue o and the Estimate $B_5(0.68)^{-5}$ (blue o) based on the fitted B_5. Red line is derived from linear comparison of the observed density to wind speed. The red lines appear curved due to the axis transformation. (For interpretation of the references to color in this figure legend, the reader is referred to the web version of this article.)

is computed from a linear fit for pure- seas defined by swell steepness $s_{sw} < 0.015$. The factor λ represents the deviation of the observed equilibrium coefficient (B_4) from the no swell case (B_0) when swell is present. We note that at very low wind speeds B_0 is near zero perhaps reflecting that at very low winds, few wind waves are generated. However, swell can occur with no wind. At low wind speeds, typically less than 3 m/s, we set B_0 to a small constant consistent with the data. We note in Fig. 15 in the 2–3 m/s wave band the value of B_4 at high steepness can be equivalent to that when the wind is 10 m/s. This suggests that some combination of processes is adding more energy into the tail than the wind.

For the Papa buoy Fig. 16 provides plots of observed λ versus U for selected swell steepness (s_{sw}) ranges along with best curve fits via a power law approximation. Fig. 17A provides the best fit curves for all swell steepness ranges at Papa to better display their form as a function of steepness. From Figs. 15 and 17-A we can conclude that the effect of swell may be parameterized by swell steepness and wind speed. At higher wind speeds (greater than 10 m/s or so), the effect is of order 10–20%. At Papa there is more scatter at lowest wind speeds which may reflect that the equilibrium range may not have a sufficient number of frequency bins to assure as good a fit or may reflect the variability of U at low wind speeds given the distance from the wind measurement. Importantly it may also represent the effect of physical parameters other than steepness. We can see no physical reason why steepness alone should control the process. Given the possible complexity of full directional spectra we think it possible that factors such the location of the sea and swell peaks with respect to each other in frequency-direction space, angular spreads, and wave versus wind angles would have some effect.

Fig. 17-B-D provide the best fit curves derived for the other three buoys using the same process as for Papa. In Fig. 17 the curves for each steepness band clearly show how the curvature changes with swell

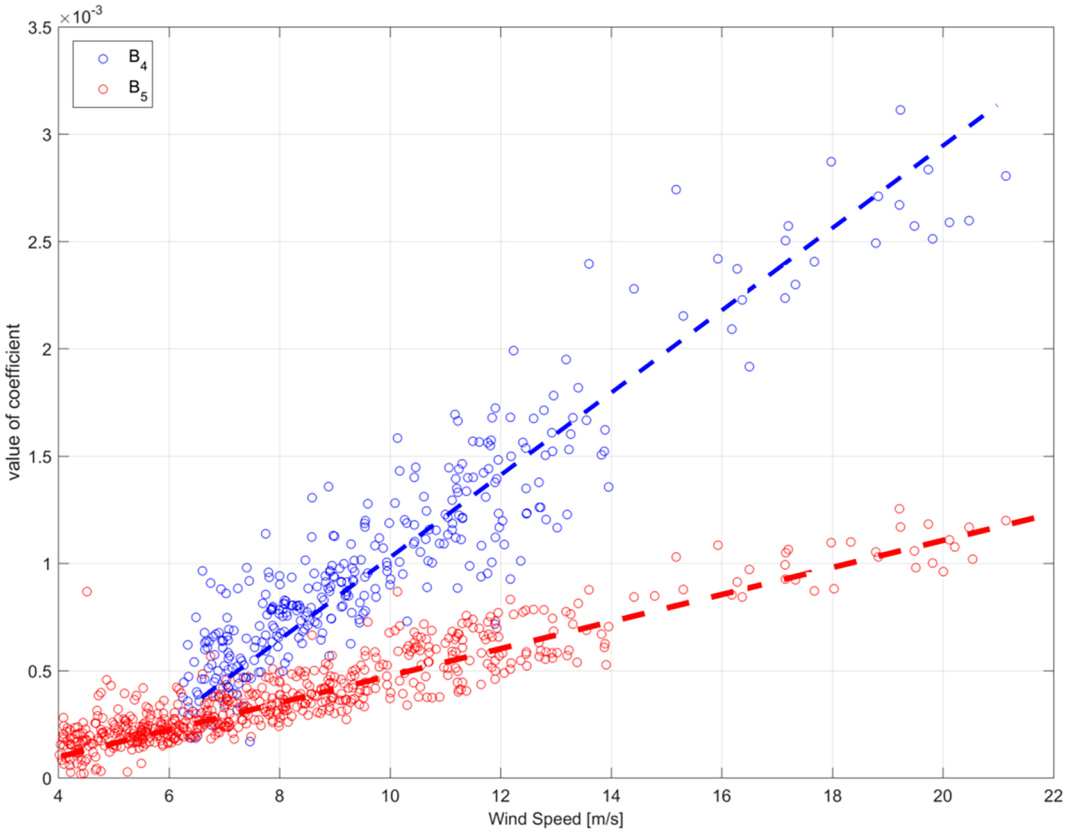

Fig. 11. Plots of the equilibrium range coefficient (B_4, top swarm) and saturation range coefficient (B_5 bottom swarm) and wind speed for Yankee. Note that B_4 has dimensions m^2-s^3 for a frequency spectrum while B_5 has dimensions m^2-s^4.

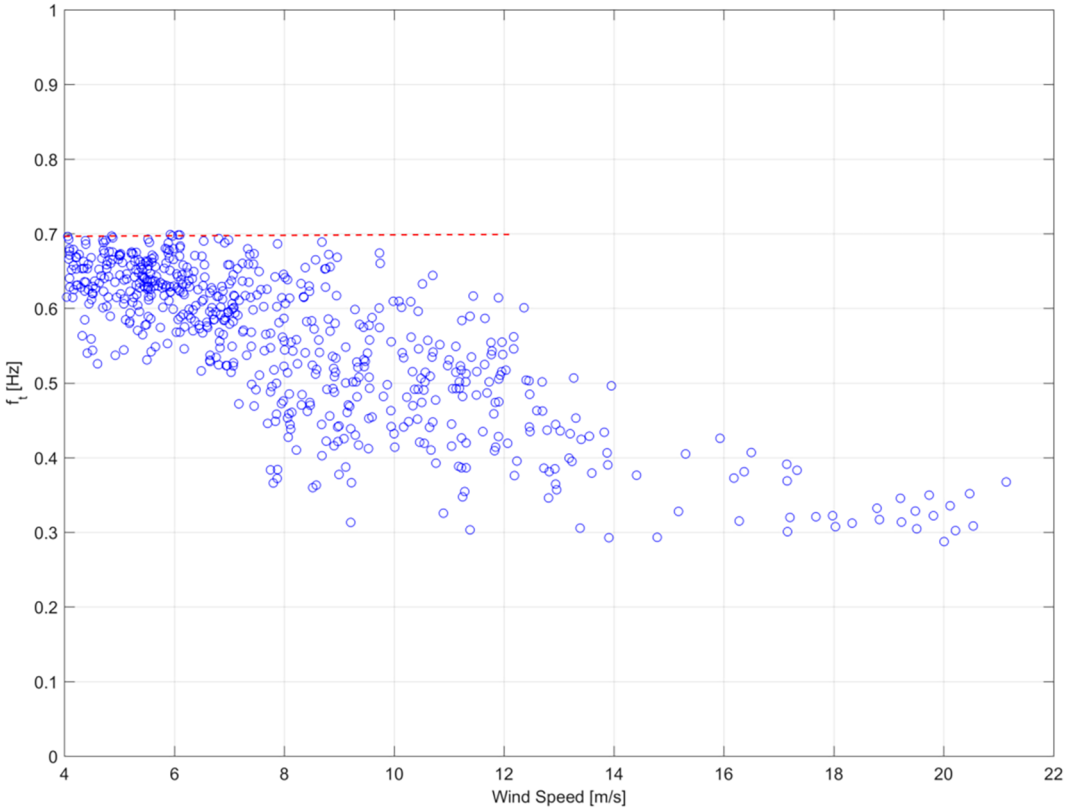

Fig. 12. Transition frequency f_t – wind speed relationship. Red dash line represents highest f_t possible given cut-off frequency for observed spectra. (For interpretation of the references to color in this figure legend, the reader is referred to the web version of this article.)

Table 2
Observed spectral tail of E(f) for field studies.

	(A) Mean ξ_m	(B) Mean σ_ξ	(C) St. Dev. ξ_m	(D) St. Dev. σ_ξ	Number
PAPA (−4 and −5)	1.0493	0.2467	0.0295	0.0545	14,920
Papa (−4 only)	0.9989	0.229	0.0146	0.0426	31,433
Yankee	1.0526	0.2652	0.0597	0.1225	804
Romeo	1.0466	0.2537	0.0513	0.1094	759
GOM99	1.0856	0.2283	0.0596	0.1065	1327
Perfect fit	1.0000	0.0000	0.0000	0.0000	

steepness. For each steepness range, the curves are similar from buoy to buoy. We note that the curves above 15 m/s for the higher steepness are determined by lower wind speeds because little data is available to constrain them above 15 m/s, so their accuracy above 15 m/s is uncertain. The effect of swell decreases with increasing wind speed, but we had no really high wind speed, high swell cases for the buoys.

3.2.2. Saturation range

The saturation coefficient B_5 was estimated independently of the equilibrium range coefficient B_4 through explicit fitting using $C(f, 5)$ defined in Eq. (22). We performed the same analysis to develop a linear fit for B_{50} the case of little to no swell following the process in Section 3.2.1. Plots of B_5 versus U were made annotated by swell steepness (Fig. 18) as done for B_4 including the line for best fit for B_{50}. The trends of B_5 with both wind and swell steepness strongly resemble the trends found in Fig. 14 for B_4 for all four buoys: as swell steepness increases at a given wind speed the saturation coefficient B_5 similarly increases above B_{50}. This is shown well in Fig. 19. We cannot go to as low a wind speed as in Fig. 15 because of the cut-off frequency of 0.6 Hz often does not allow data points to get a good fit for B_5. The dimensions of B_5 are m^2–s^{-4}.

We note that the relation $B_5 = f_t B_4$ suggests that if f_t varies over a narrow range B_5 and B_4 would be correlated. Fig. 20 displays the degree to which this is true. The points in the plot are annotated by swell steepness and the data indicates that goodness of fit seems the same no matter the sea-swell composition. The coefficient in the linear fit for the line of agreement tends to be approximately the average of f_t in each data set.

Figs. 18–20 document that B_5 not unlike B_4 varies with wind speed and swell steepness. We find this interesting because the different ranges are presumably due to dominance of a different combination of processes. We had an expectation that our data might exhibit full saturation noted by Tamura et al. (2014) and Lenain and Melville (2017) at high frequencies and high wind speeds, but our data did not show this. Our maximum wind speeds were almost 20% larger than Tamura et al. (22 versus 18 m/s) and our friction velocities and wave heights were 1.4 m/s and 6.5 m versus Lenain and Melville (2017) maximums of 0.4 m/s and 2.5 m. It may be that highest frequency we can observe is only equivalent to 4 rad/m and too low to see it. It could also be that at the highest frequencies the effects of Doppler shifts contaminate our spectra. We do note however in almost of our spectra the saturation range appears to be f^{-5} at least to a frequency of 0.9 Hz.

The clear dependence of B_5 and B_{50} on wind speed is inconsistent with Phillips (1958) original hypothesis for the –5 power range in that his coefficient was a constant. But data from 4 buoys consisting of 2 instruments types, processed via 2 different spectral analyses in 3 different environments shows some dependence. Moreover, it is the energy level itself in frequencies in the saturation range as shown in Fig. 10. that vary with wind speed. Forristall (1981) pointed out that in the Pierson-Moskowitz spectrum the higher frequencies scale with speed, and since the JONSWAP spectrum is directly related to this shape it too has a –5 power law tail in the higher frequencies. Thus, it may be that what we term the saturation range is not just defined by

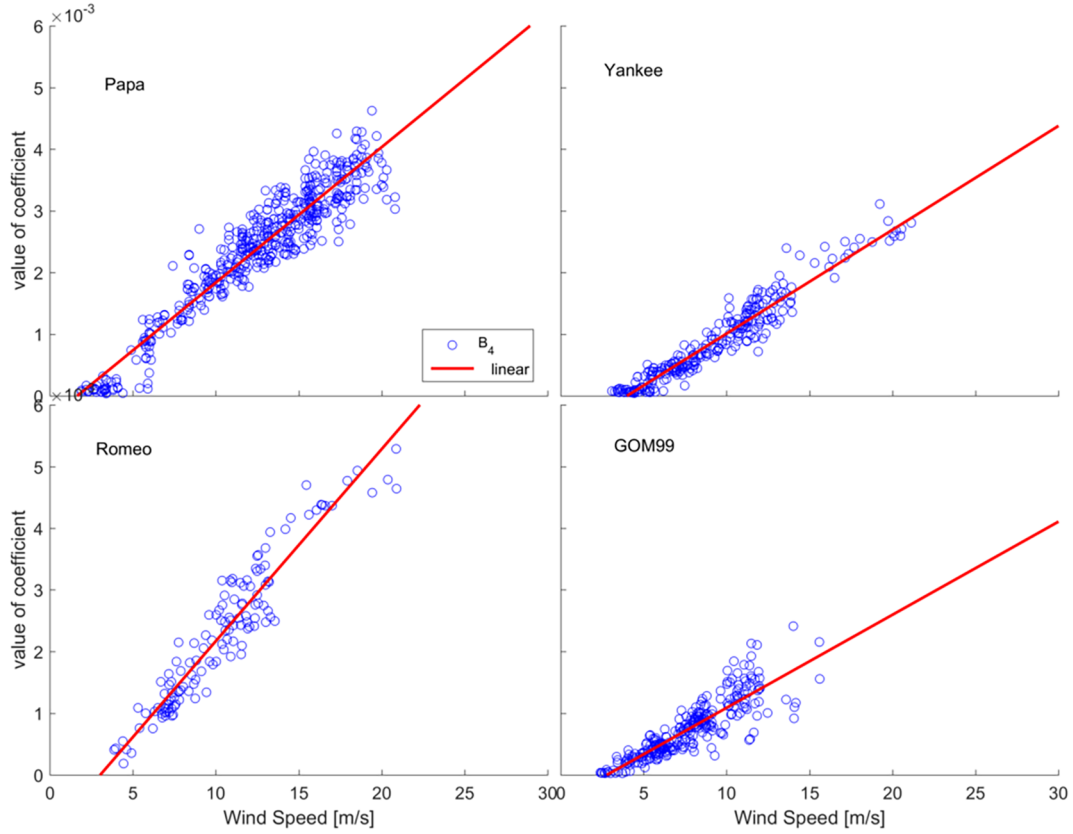

Fig. 13. Relationship between the equilibrium range coefficient B_4 and wind speed U for pure wind sea cases (swell steepness less than 0.015). Red line is linear regression for the data set. For the pure wind-sea case B_4 will be termed B_0. The dimensions of B_4 are m^2-s^3. (For interpretation of the references to color in this figure legend, the reader is referred to the web version of this article.)

breaking alone but has a complex source term balance different from the –4 power equilibrium range with the transition frequency representing a shift in process dominance.

3.3. High energy swell spectra

We now consider the cases where swell is very dominant: R > 90% with U < 6 m/s. Using data from a single buoy (Romeo) in the SW06 Experiment, we look at two cases. Fig. 21 contains compensated spectra where swell occupies most of the tail of the spectra out to 0.9 Hz. The winds are less than 2 m/s. Fig. 22 contains compensated spectra for other very swell dominant cases but with somewhat higher wind speeds of 4–5 m/s. In Fig. 22 half of the tail of the spectrum is wind-sea.

Both Figs. 21 and 22 show that a −4 power law range extends well into the swell portion of the spectrum. In Fig. 21 where swell is dominant over much of the tail, the −5 power law range also exists in the swell frequency bands. The −4, −5 power-laws were originally developed for 'pure' wind-sea spectra. In wind-sea spectra, the −4-power law is associated with the equilibrium range concept where the nonlinear source term dominates spectral shape Kitaigorodskii (1983) or with Phillips's (1985) concept of a source term balance. But in the high energy swell cases, the −4 and −5 power law range can exist in the swell band where there may be wave-wave interactions but there is no wind input, although we may suppose that there might be occasional breaking. This suggests that the −4 and possibly −5 power laws exist independent of wind, supporting the Kitaigorodskii explanation for the equilibrium range because the wave-wave interactions are present in all spectra. At a minimum, it suggests that we still do not fully understand how the power laws manifest from the underlying physics.

In Fig. 22 we focus on cases where swell is dominant, but a significant portion of the spectrum is still wind-sea (winds 4–5 m/s). In Fig. 23 the compensated spectrum for the −4 power-law is shown and we have divided the −4 range in two parts, split at the sea-swell boundary. We use the notation B_{sw} to denote the −4 power-law coefficient for the swell side and B_{se} for the wind-sea side. We can calculate B_{sw} for the −4-power law by adapting the compensated spectra to go from 1.25 f_{sw} to f_s, where f_{sw} is the swell peak. We also estimate B_{se} in a similar fashion for the range from f_s to the highest observed frequency where the −4 power level holds. B_{se} and B_4 may not have exactly the same value because the low frequency definitions are different (f_s versus $1.25f_{psea}$). Importantly, the −4 power-law appears continuous across f_s, since B_{se} is about equal to B_{sw}.

In the 'pure' wind-sea case, we expect that the coefficient B_4 to be linearly related to wind speed. Plots of B_{sw} against U for all four buoys yielded an almost flat slope with great scatter confirming no strong relationship to wind, which is not unexpected because these are basically swell spectra. The question then is what factor controls both B_{sw} and B_{se} for wave states that are strongly swell dominant, because the wind-sea just looks like the tail of the swell having no independent sea peak.

A key parameter in wave physics is steepness. For high swell dominance we plot B_{sw} against the swell steepness s_{sw} (Fig. 24) for each buoy. All show strong relationships quadratic in nature. Fig. 23-C shows that B_{se}, which is computed only over wind-sea frequency components is also related to swell steepness. These results lead to the conclusion that the tail of the large swell spectra at lower wind speeds (R > 90% U < 6 m/s) follow the −4 and −5 power laws but their coefficients dependent on swell steepness not wind speed. We underscore that this is true only for a very specific subspace of sea and swell combinations. This in turn suggests that the power laws for the tail of the wave spectra tend toward two asymptotes, wind dominated (B_4 related closely to wind speed) and swell dominated (B_{sw} and B_{se} related closely to swell

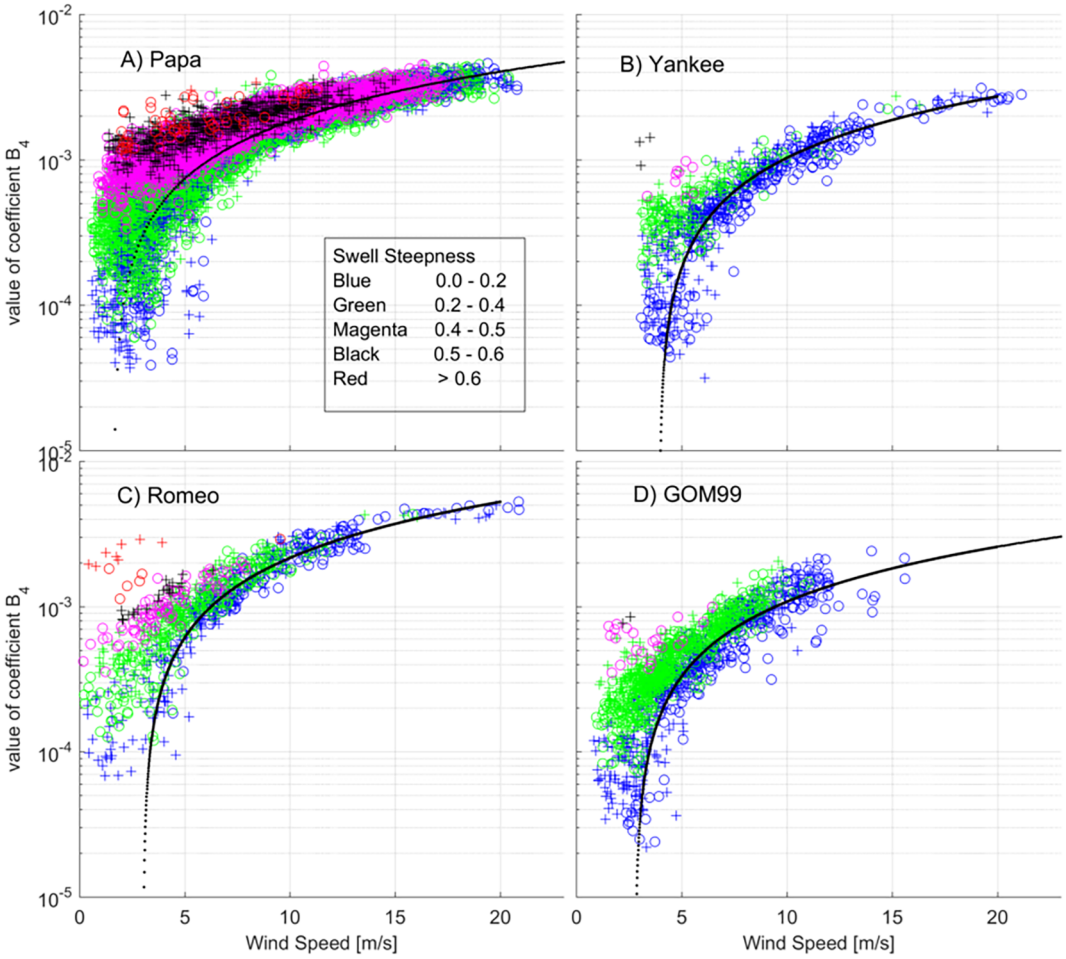

Fig. 14. Relationship between equilibrium range coefficient (B_4) and wind speed (U) for all spectra. The value for B_4 is plotted against U with the color symbol reflecting the value of swell steepness. The dark black line represents the linear relation derived for B_o versus U. The dimensions of B_4 are m^2-s^{-3}.

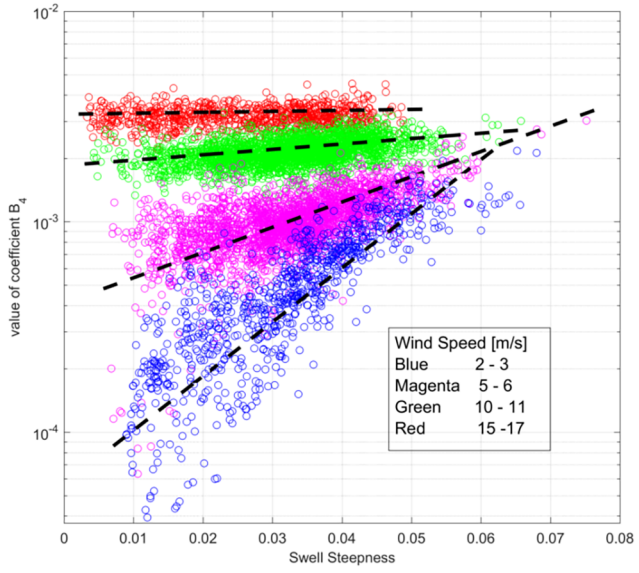

Fig. 15. Equilibrium range coefficient B_4 and swell steepness. B_4 within specific wind speed ranges is plotted against swell steepness at Papa. Dash lines are trends through the data centroid.

steepness), with many spectra falling in a mixed regime.

Examination of the spectra of very large swell at low wind speeds generally show a single peak with a shape similar to a 'pure' wind-sea, but with almost energy in the swell part of the spectrum. For the Ocean Station Papa and Romeo buoys, we show examples of wave spectra with large swell at low winds matched (by wave height and peak frequency) to corresponding spectra at high winds with little swell. The plots of the frequency spectra (Fig. 25) show the complete set of spectra from each buoy matching the requirements. The high swell-low wind, low swell-high wind spectra lie overtop each other, tails included, indicating that the large swell spectra have a shape comparable to the wind-sea.

Hasselmann and Hasselmann (1985) indicate that spectra with same total energy and peak frequency have similar S_{nl} if they have similar directional distributions. It does not matter whether the waves are sea or swell. The equivalence of the tails of the two sets of spectra suggests that the transfer by the nonlinear source term in the large swell-low wind case is sufficient to maintain the same energy levels in the tail equivalent to the 'pure' wind-sea case even though the wind input in the sea case is far larger. Here the swell cases had winds of 2–4 m/s while the wind in the wind-sea spectra is 12–16 m/s. Thus, it appears the S_{nl} in the swell case is equivalent to having forcing by a 12–16 m/s wind. That the spectral shapes are so similar supports to Kitaigorodskii's (1983) contention that a f^{-4} range like the equilibrium range is determined by the dominance of S_{nl}.

We conclude that large energy levels in the tail of the large swell-low wind case are pumped there via S_{nl}. This suggests that in less swell dominant cases S_{nl} may also be the principal mechanism causing the modulations of the energy level in the tail. This provides a direct, physics based, link between the swell and the tail of the spectrum. When the directional spectrum is complicated (multiple swell peaks, differing angles between the swell components and the sea component),

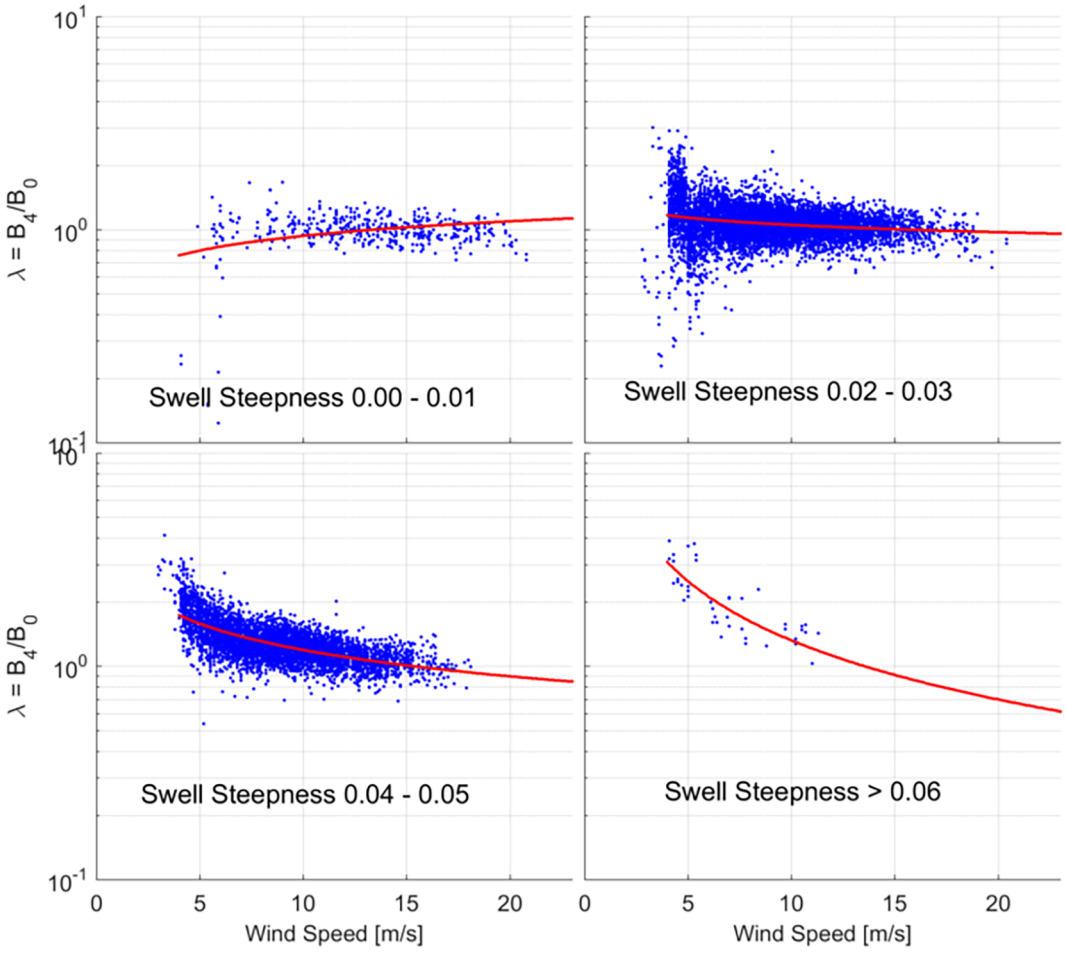

Fig. 16. Plot of $\lambda = B_4/B_o$ versus wind speed at Papa for swell steepness ranges.

energy flux due to S_{nl} may also have a complex structure. This may help explain the variability in stress estimates often noted when swell is present. However, direct proof of the role of S_{nl} will require extensive computations beyond the scope of this paper.

3.4. Transition frequency f_t from the equilibrium to saturation range

The transition frequency between the -4 and -5 power law segments of the tail of the spectra has been hypothesized to mark the change from dominance by the resonant nonlinear interactions to that dominated by breaking. Here we examine its relationship to wind speed and swell steepness.

We can compare our estimates of f_t to the Lenain and Melville (2017) data set and Phillips (1985) scaling by using the linear theory estimate of

$$k_t = (2\pi f_t^2)/g \tag{27}$$

Lenain and Melville (2017) observe the transition wave number k_t and compare it to Phillips (1985) expression

$$k_t u_*^2/g = r \tag{28}$$

finding values of r between 0.01 and 0.025. The mean of the data appears near 0.015.

During GOM99, the atmosphere was usually neutral. We can use linear theory to estimate k_t from f_t. We selected cases in the 'pure' wind-sea regime and used the measured u_* values to compute r values yielding a mean r = 0.013 (standard deviation 0.0027, 93 samples) which agrees well with Lenain and Melville (2017). The same can be done for SW06 (Romeo and Yankee buoys) where the boundary layer is usually very stable for most of the sample period. When combined with GOM99 buoy values, the mean r is 0.012 (standard deviation 0.0927, 217 samples). Where we can measure u_* our data base of more than 200 spectra yields r comparable to Lenain and Melville (2017). This helps validate the Lenain and Melville (2017) values, but moreover it suggests that the f_t values we derived from our spectral-tail fitting process are consistent with other data sets adding a measure of validation to our values.

Assuming linear theory $k_t \frac{u_*^2}{g} = r$ can be algebraically transformed to a frequency form $\frac{u_* f_t}{g} = \frac{r^{1/2}}{2\pi} = R_*$ (R_* would be about 0.019 for a r of 0.015) using R_* to indicate the $\frac{u_* f_t}{g}$ version We can compute this easily for the GOM99, Romeo and Yankee getting R_* of 0.0165 standard deviation 0.0174.

It is also possible to consider a different normalization using U and f_t: $\frac{U f_t}{g} = R_u$ which would also allow us to include Papa into the data set. Selecting from the low swell regime, we can compute R_u for GOM99, Romeo and Yankee getting 0.5314 (standard deviation 0.0927). If we assume that we can approximate u_* by $c_o U$, we can compare the R_* and R_u forms by R_u R_*/c_o. It depends upon buoy and wind speed range but our measured c_0 ranges from 0.03 to 0.04 for mid wind-speed ranges which yields a range of in R_u of 0.47 to 0.63; using $c_0 = 0.035$ gives 0.54. We conclude that using R_u is equivalent to R_*. We can now include Papa data into the analysis and find that $R_u = 0.5418$ with standard deviation of 0.0763 for 447 samples. This also suggests that our fits for the Papa data are consistent with the other data sets.

The effect of swell on the transition frequency can now be investigated in terms of R_u. We estimate what the 'pure sea' value R_{uo} by

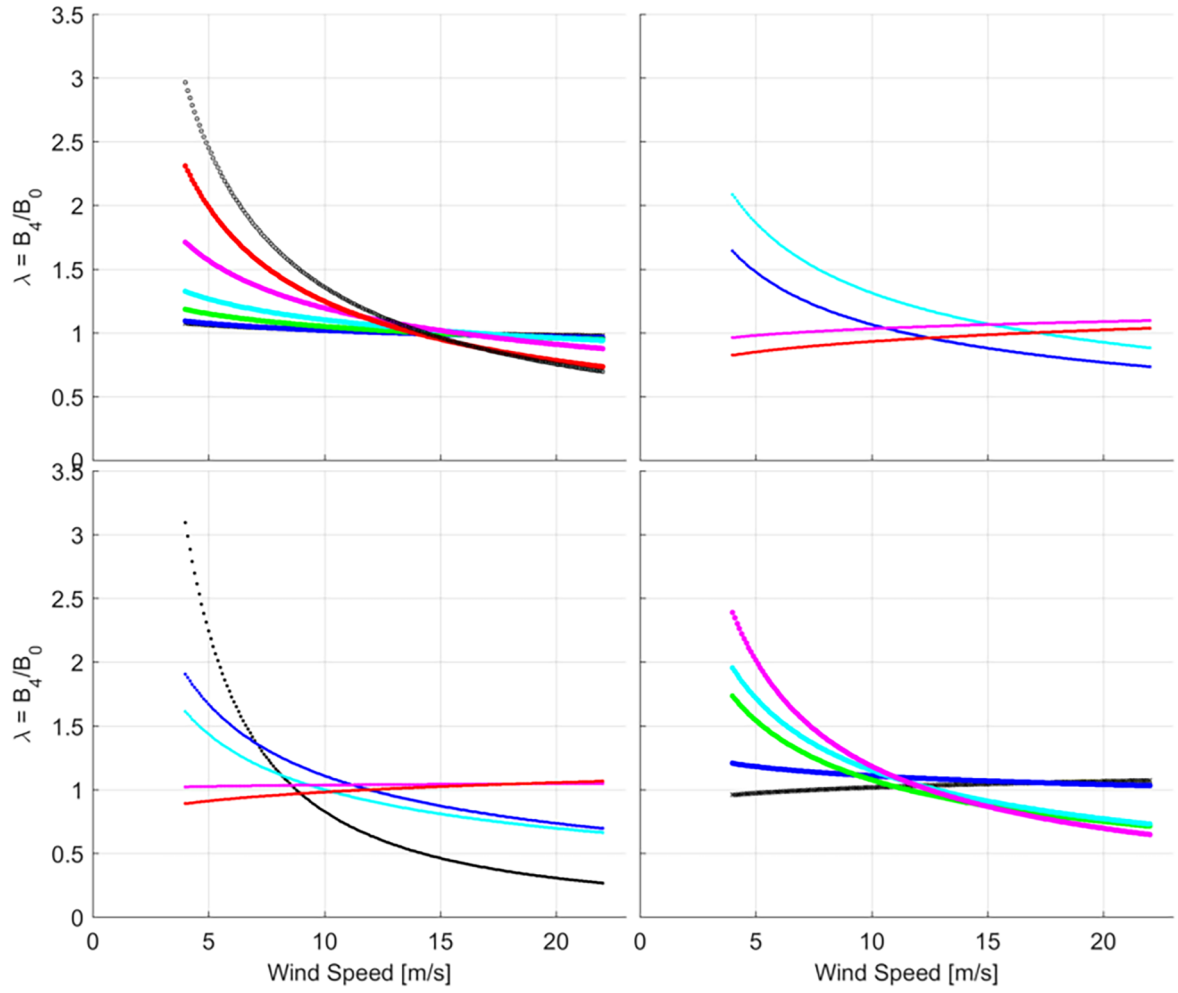

Fig. 17. Plot of fitted λ curves for each buoy by swell steepness. Heavy black line 0.00–0.01, blue 0.01–0.02, green 0.02–0.03, cyan 0.03–0.04, magenta 0.04–0.05, red 0.05–0.06, and light black > 0.06. Curves beyond 15 m/s may be unreliable due to lack of data for higher steepness. (For interpretation of the references to color in this figure legend, the reader is referred to the web version of this article.)

averaging as we did above for each buoy. Then for each buoy we tag the spectra that fall into specific swell steepness ranges and estimate the mean $<R_u/R_{uo}>$ for each steepness range. We plot these as curves in Fig. 26 by buoy. Given that U is not measured in the same way nor the effects of atmospheric stability removed, the four curves still have a similar trend: as swell steepness increases the value of $<R_u/R_{uo}>$ consistently decreases. Indeed if normalized by the value at steepness of 0.01 the curves would almost overlue each other. This would indicate that the presence of swell tends to shift the transition frequency lower (i.e. towards the spectral peak) than the 'pure wind-sea' value for a given wind speed. Thus, all three parameters of the spectral tail B_4, B_5, f_t are functions of both wind speed and swell steepness at least over the frequency ranges we observe.

3.5. Wind, sea and swell direction

Analysis of mean directional properties at the Papa buoy provides insights significant to our finding. We compute (1) the mean direction θ_{sw} for the swell portion of a spectrum and (2) the mean direction θ_{se} for the sea-tail portion of the spectrum that is in the equilibrium range and higher frequencies (f > 0.4 Hz). The wind direction is θ_w.

In the top panel of Fig. 27 we compare the sea-tail θ_{se} and swell directions θ_{sw} with points colored according to swell steepness. The cases where the sea-tail and swell directions are close usually represent cases where the sea state has developed from winds from one direction, but where the wind speed then dropped while not changing direction. The figure also shows that swell often comes at the significant angles to the wind-sea over the full ranges of wave steepness. In the bottom panel of Fig. 27 the subset of data with R > 95% shows similar patterns.

In Fig. 28-A we plot the mean direction θ_{se} of energy in the sea-tail versus the mean wind direction θ_w with the data points colored by swell steepness. The mean direction of wave energy in the sea–tail is very close to the mean wind direction no matter the swell steepness or swell direction with few exceptions. In Fig. 28-B we restrict the data to R > 95% and low wind speeds, i.e. large swell dominance. The pattern remains about the same as Fig. 28-A. The 33,000+ observations from the Papa buoy document the high degree to which the two means agree, regardless of swell steepness, direction, and swell dominance. Even in the case of high amplitude, high steepness swell that occupies almost all of the observed spectral bandwidth, the direction of energy in the wind-sea tail has the direction of the wind, even though its energy level appeared controlled by swell steepness. In these cases, the concept of a swell generated wind of Harris (1966) may suggest that in these cases the swell will drive the wind in the direction of propagation, yielding a correlation.

The Papa buoy data does not permit us to study the lobe structures of the directional spectrum, so we cannot say that directional distribution remains the same between sea and swell dominant cases. However, we can conclude that whatever they are, the mean energy directions in the sea tail are close to the wind direction regardless of sea or swell mixture. We will assume that having the mean direction of energy in sea-tail in such close agreement to the wind direction when

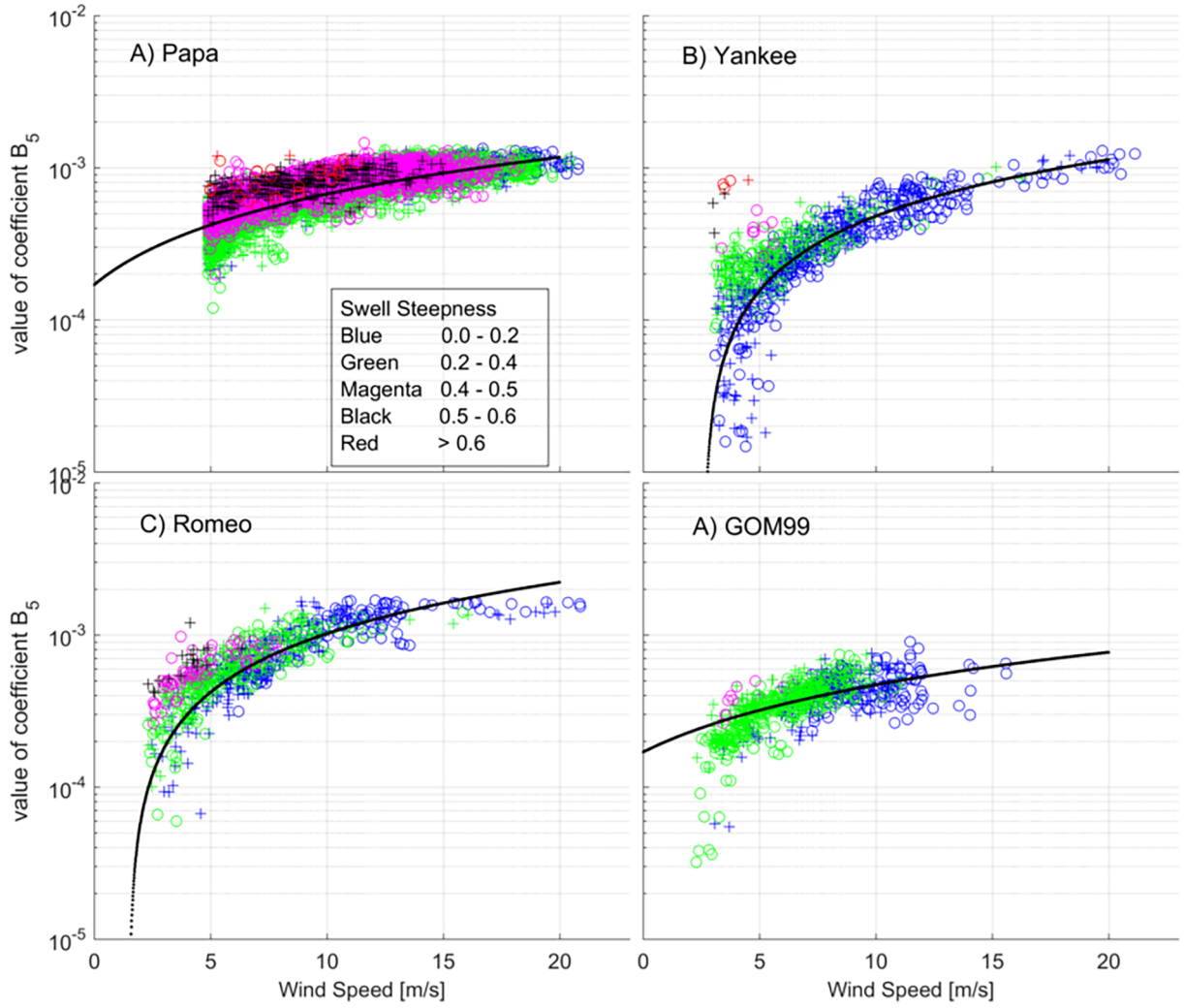

Fig. 18. Relationship between saturation range coefficient (B_5) and wind speed (U) for all spectra. The value for B_5 is plotted against U with the color symbol reflecting the value of swell steepness. Black line is the relationship B_{50}- U. The dimensions of B_5 are m^2-s^4.

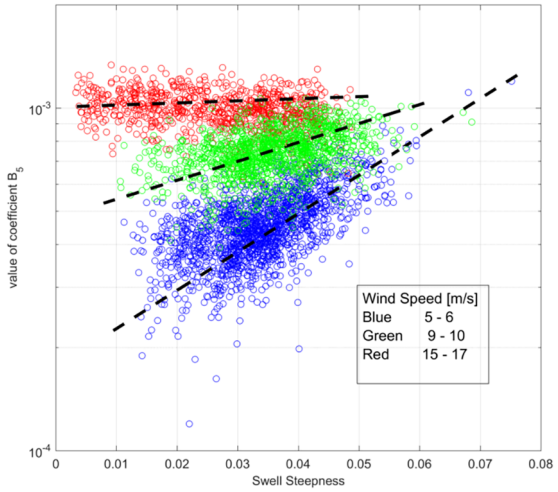

Fig. 19. Saturation range coefficient B_5 and swell steepness. B_5 within specific wind speed ranges is plotted against swell steepness at Papa. Dash line is trend through data centroid.

swell is present implies that there is little energy in the half-plane opposite to the wind. Perhaps future studies with high resolution directional spectral measurements will lead to further insights. Though not presented here, our data shows that in cases where there is a more distinct wind-sea peak at f < 0.4 Hz, there is often a transition over the frequencies between f_s and 0.4 Hz from the swell direction to the sea directions perhaps equivalent to the merger effect cited by Collins et al. (2018).

3.6. Discussion of results concerning the spectral tail

The key question Section 3 sought to answer was if the mathematical formulism of a two power-law spectral tail, which appeared to work well for wind-seas with little swell could be applied to describe spectra that have significant levels of swell energy. Our results clearly establish that the spectral tail equation Φ can be used to easily fit hybrid sea-swell spectral tails yielding the triplet [B_4, B_5, f_t] as parameters. Analyses showed that when swell steepness was low the relationships between wind speed and each of B_4 and B_5 were linear with wind speed but established that as swell steepness increased the values of B_4 and B_5 increasingly deviate from the 'pure wind-sea' value. The transition frequency f_t could be converted into an equivalent wave number k_t which in the case of no swell compared well to the dimensionless values $k_t \frac{u_*^2}{g}$ found by Lenain and Melville (2017). The equivalent in frequency is $\frac{Uf_t}{g}$ which can be used to predict the transition period $(\frac{Uf_t}{g})_o$ for low swell conditions and then show that the presence of swell decreases f_t to longer waves. We note again that in our data sets the saturation

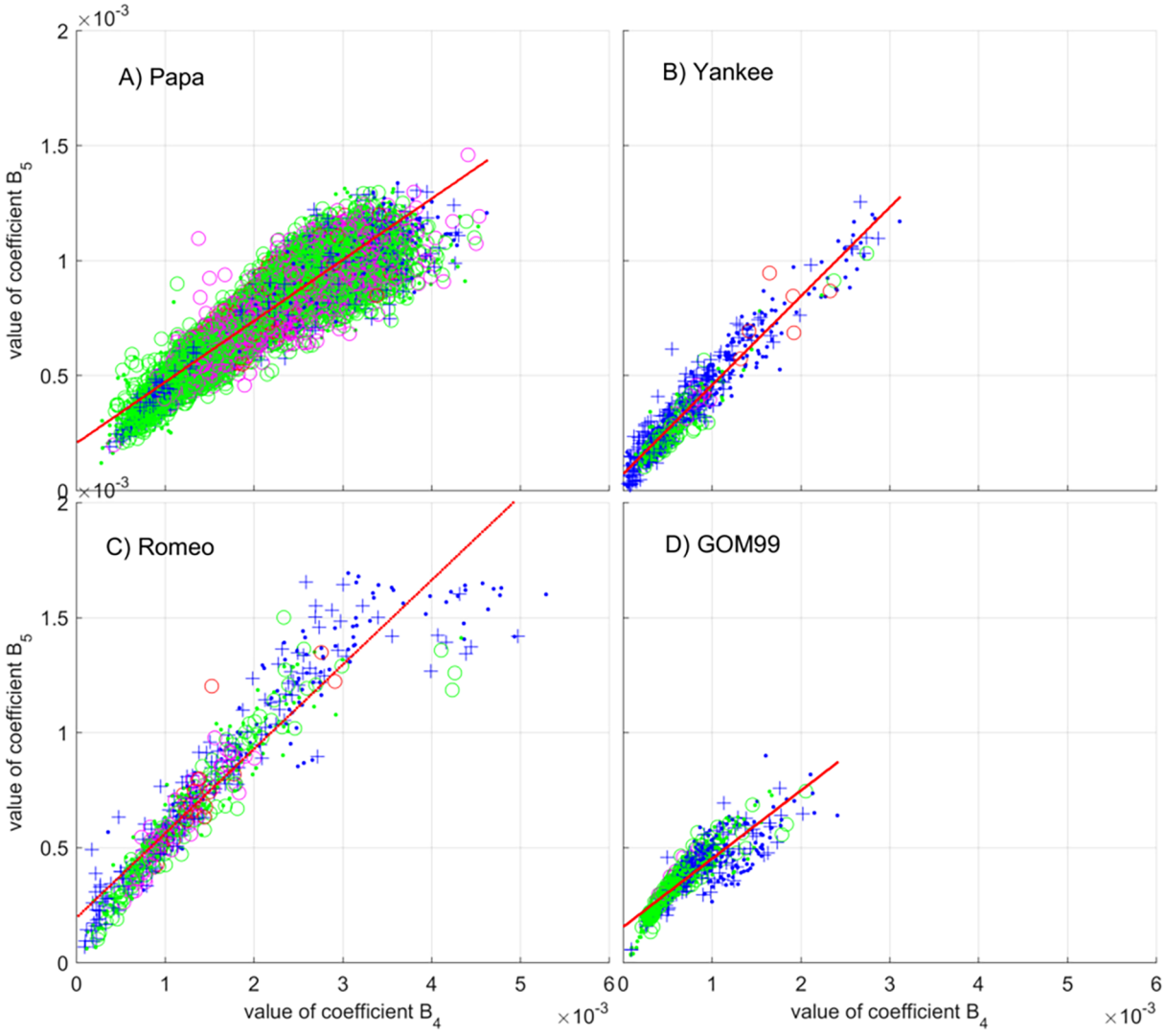

Fig. 20. Comparison of equilibrium B_4 and saturation B_5 coefficients for each data set annotated by swell steepness; 0–0.01 blue dot, 0.01–0.02 blue +, 0.02–0.03 green dot, 0.03–0.04 green o, 0.04–0.05 magenta o, 0.05-,08 red o. (For interpretation of the references to color in this figure legend, the reader is referred to the web version of this article.)

coefficient is not a constant as was implied by Phillips (1958) but also we did not appear to reach frequencies where full saturation occurred. Our data appears to more closely match that of Tamura et al. (2014) excepting we did not reach the fully saturated regions.

The data show that [B_4, B_5, f_t] all are functions of wind speed, although B_4, and B_5 are more strongly influenced than f_t and the deviations from the 'pure' wind-sea cases appears related to swell steepness. Analysis of wind and wave directions indicated that overwhelmingly the direction of the waves in the far spectral tail was in the direction of the wind. In summary we conclude that swell impacts the tail of the wind-sea spectrum and that the deviation away from the 'pure' wind-sea appears strongly related to the swell steepness, but decreases as the wind speed increases.

When energetic 'pure' sea and 'pure' swell spectra are compared for the same height and peak period, the spectra are very similar; if the color coding for sea and swell were to be removed it would be hard to differentiate between them. In the large swell case, there is almost no wind input, yet the equilibrium range is the same as the wind-sea where the winds were 12–16 m/s. This suggests that it is the Hasselmann interactions S_{nl} that transport the energy into the tail frequencies suggesting that the modulation of spectral tail by the swell may be largely due to the role of S_{nl}. There is a good deal of variance still left and it could well be that the impact of other spectral parameters (number of swell peaks, relative sea and swell steepness, and angles between swell and sea) may be needed to understand the interaction more fully. If S_{nl} is of significance, the details of spectral shape become important.

4. Effect of swell induced roughness modulations on stress

Analysis of the impact of swell on the spectral tail indicated that the swell steepness modulated the energy level of the tail by significant amounts. We consider a simpler problem: estimating the potential effect of the swell modulation of the short waves on stress. While swell acts directly on the wind field by creating a wave-driven component via the upward momentum transport and likely altering the lower wind profile, our data suggests that swell also modulate the energy level of the tail compared to the 'pure' wind-sea case, probably via the nonlinear source term S_{nl}. Since the energy level of the tail is an indicator of the roughness of the sea surface, it seems plausible that the swell induced amplification or damping of the energy of the spectral tail could modulate the stress. This offers an additional mechanism for modifying momentum transfer via the tail of the spectrum not previously considered where the swell impact is limited only to the long-wave part of the spectrum. Importantly we note that this extra drag would only be

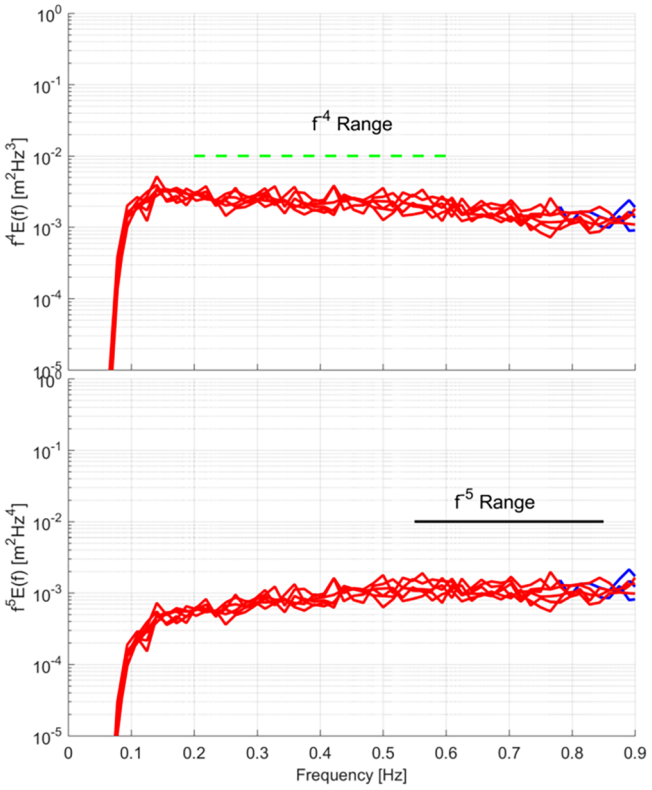

Fig. 21. Compensated spectra at Romeo for high energy swell spectra with low windspeeds (U < 2 m/s). Swell bands are in red, wind sea in blue. Wind sea component typically lie at frequencies lower than 0.75 Hz. The region of the spectra beneath the flat green dashed line is proportional to f^{-4} analogous to a wind-sea equilibrium range but it lies completely within the swell band. In the lower panel the part below the black line is proportional to a f^{-5} range but it lies largely in the swell. Frequency in Hz. E(f) in m^2-s. (For interpretation of the references to color in this figure legend, the reader is referred to the web version of this article.)

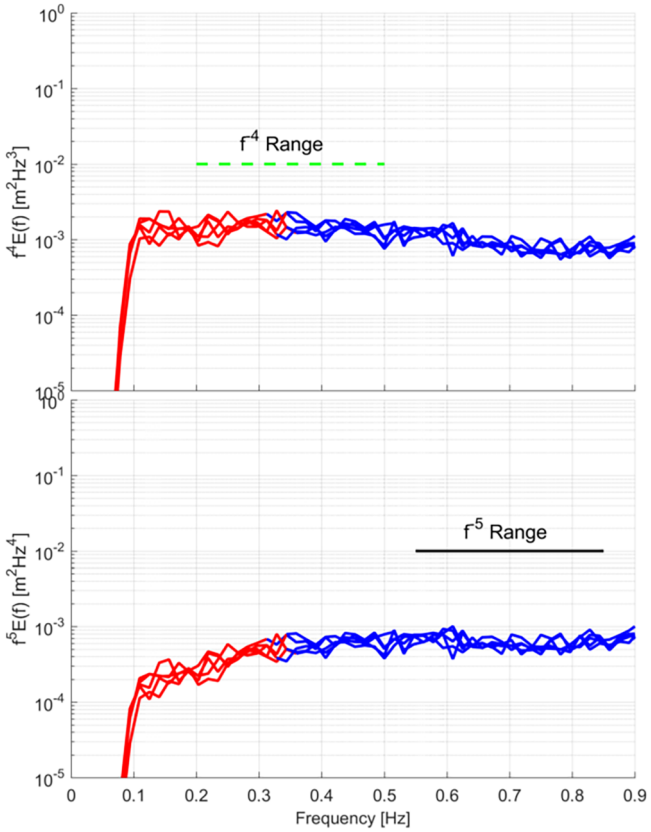

Fig. 22. Compensated spectra at Romeo for hybrid sea-swell cases. Spectra are swell dominant (R > 90%) with moderate windspeeds (U 4–6 m/s). Legends are as in Fig. 21. In the upper panel the −4 power-law range begins in the swell band and extends a long way into the sea band. In the lower panel the −5 power-law range is within the wind sea range. Frequency in Hz. E(f) m^2-s.

there as a consequence of the swell and should be counted as a swell contribution in addition to any direct action in the long waves.

4.1. Background

The literature on the impact of swell on drag is especially large (e.g. Harris, 1966, Donelan et al., 1977, Smedman et al., 1999, Grachev et al., 2001; Smedman et al., 2003, Garcia-Nava et al., 2009, Pan et al., 2005, Sullivan et al., 2008, Smedman et al., 2009, Sahlee et al., 2012, Högström et al., 2013, 2015, Potter, 2015, Jiang et al., 2016; Kahma et al., 2016, Högström et al., 2018 among others). For wind-seas the drag on the atmosphere is often attributed to the shortest waves on the sea surface, lying in what we have termed the tail of the wind-sea spectrum. Donelan et al. (2012) suggests that characterization of the drag requires inclusion of wave frequencies greater than 10 Hz. The main effect of swell is thought to be the transfer of momentum from the long swell waves into the atmosphere in the direction of the swell creating a wave-driven wind-component along the lines of Harris (1966) (Donelan et al., 1997, Drennan et al., 1999, Smedman et al., 1999, Grachev et al., 2001, Fairall, 2001, Kudryavtsev and Makin, 2004, Högström et al., 2013, 2015, 2018 among others). The result is that the near surface flow associated with the swell may be in opposition or addition to that being driven from above. Observations indicate that when is swell is present, the wind velocity profile does not appear to follow Monin-Obukv Similarity (Drennan et al., 1999, Smedman et al., 1999, Drennan et al., 1993, Högström et al., 2013, Högström et al., 2013 among others). Numerical simulations (e.g. Sullivan et al., 2008 and Jiang et al., 2016)) indicate modifications to the log-profile in the lower boundary layer induced by the swell.

Determining the fraction of the stress attributed to long wave motions versus the more standard model of drag by small scale roughness attributed to the short waves is complicated. This paper adds a new wrinkle into the problem by demonstrating that the swell, also modulates the roughness normally attributed to the shorter waves. That long-waves and short-waves interact is in no way new, what the study amplifies is a level of predictability in the spectral formulation explicit to the wind-sea/swell divide. A field study at low to moderate wind speeds by Grare et al. (2013) finds in a mixed sea-swell regime that where swell is present typically more than 90–95% of the downward momentum is supported by waves shorter than 3 s and that for older wave ages the upward momentum is at most 20% of the downward momentum. Other studies find differing proportions most likely due to differences in wind-sea, swell and wind conditions.

4.2. Development of a swell modulated equation for stress

The spectral results derived in Section 3 parameterize the spectral tail for the full range of sea and swell conditions because in principle [B_4, B_5 and f_t] can be predicted if U and swell steepness are known. We can then directly specify the spectrum in the region in the high frequency tail and compute the momentum transfer from the atmosphere to the waves in the tail due to the swell perturbation using Donelan et al.'s (2012) approach. In order to understand whether the swell modulation is important, we neglect the long wave components allowing us to see if significant differences occur by comparing the predictions with swell modulation to those without. Selection of 0.33 Hz as

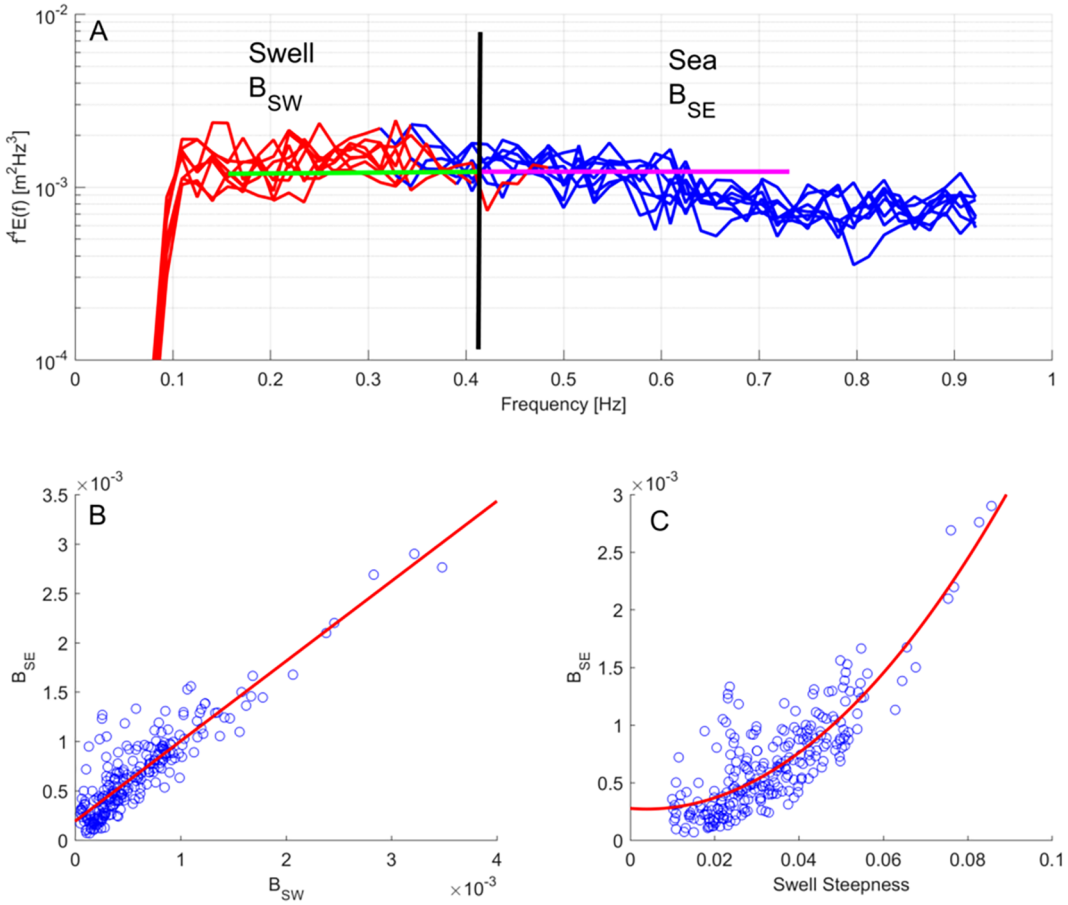

Fig. 23. The -4 power law range of high swell, moderate wind speed spectra from Romeo. Panel (A) shows the -4 power law coefficient (B_{sw}) for the swell part and (B_{SE}) for the sea part. Panel (B) is a plot of B_{SE} versus B_{sw} showing that the -4 range is essentially continuous across the sea-swell divide. Panel (C) shows that B_{se} is related to swell steepness.

the upper bound for the tail frequencies comes from Grare et al. (2013) and is appropriate for oceanic wave states at moderate fetch and durations. For other conditions a different frequency may be more appropriate. We note that there is some discussion that the saturation range may at some point become 'fully' saturated though we did not observe this given the frequency range of our data. We will ignore the possibility of full saturation (as does Donelan et al., 2012) under the assumption that most input occurs before this point.

Following Donelan et al. (2012), absent currents, the momentum input to the waves is $S_{in}(U, f, \theta)/C(f)$ where S_{in} the energy input at a frequency f and direction θ and C is the celerity of the waves at that frequency. We express the input in terms of wind speed since we wish to solve for u_*. Donelan's equation becomes

$$u_*^2 = \rho_w/\rho_a g \iint \frac{S_{in}(U, f, \theta)}{C(f)} d\theta df \tag{29}$$

We can break the directional spectrum into three segments as in Rieder and Smith (1998): E_{sw} the portion in the swell frequency band (0 to f_s), E_{hf}, the portion in the high frequency tail (here taken from 0.33 Hz and higher), and E_{mf}, the mid-frequency portion between the swell cut off and the tail. The total stress u_*^2 can then be divided into three components

$$u_*^2 = [u_*^2]_{sw} + [u_*^2]_{mf} + [u_*^2]_{hf} \tag{30}$$

corresponding to the frequency divisions with each obtained from

$$\rho_w/\rho_a g \iint \frac{S_{in}(U, f, \theta)}{C(f)} d\theta df \tag{31}$$

over the appropriate frequency intervals. Normally $[u_*^2]_{sw}$ is upward and $[u_*^2]_{hf}$ is downward. $[u_*^2]_{mf}$ is often neglected.

In order to estimate the impact of the swell induced modulation of the tail, algebraically we will assume that $[u_*^2]_{hf} \gg [u_*^2]_{sw} + [u_*^2]_{mf}$, noting that $[u_*^2]_{hf}$ contains that due to wind input and the swell modulation. We can understand the relative role of direct wind input and swell modulation by comparing cases with and without swell. We develop an equation for $[u_*^2]_{hf}$ (which we will call u_{*s}^2 for notational simplicity) and compare it to an estimate of the stress when little swell is present u_{*o}^2. We reemphasize that the neglect of the other terms is only for purpose of developing an estimate of the stress due to the tail. We do not imply that the neglected terms are unimportant.

Expressions for S_{in} in deep water for high frequency waves with no current such as those by Miles (1957) or Plant (1982) are of a form

$$S_{in0}(U, f, \theta) = \Pi \times \cos(\theta - \theta_w) \times E(f, \theta) \tag{32}$$

where Π is a function of f and U^m or u_*^m with m = 1 or 2. Sheltering coefficients can be included, but here they are not needed because we are in the shorter wind wave regime where they may be assumed similar. The algebraic use of an unspecified function Π simply allows us to carry which ever form desired without having to explicitly write it down, because it is ultimately factored out. The factor $(\theta - \theta_w)$ is the difference between the wave propagation direction and wind direction. We rewrite

$$E(f, \theta) = E(f) \times D(f, \theta) \tag{33}$$

where $D(f, \theta)$ is a directional spreading function with the property that its integral over angle space is 1 for each f. Our formulation of the

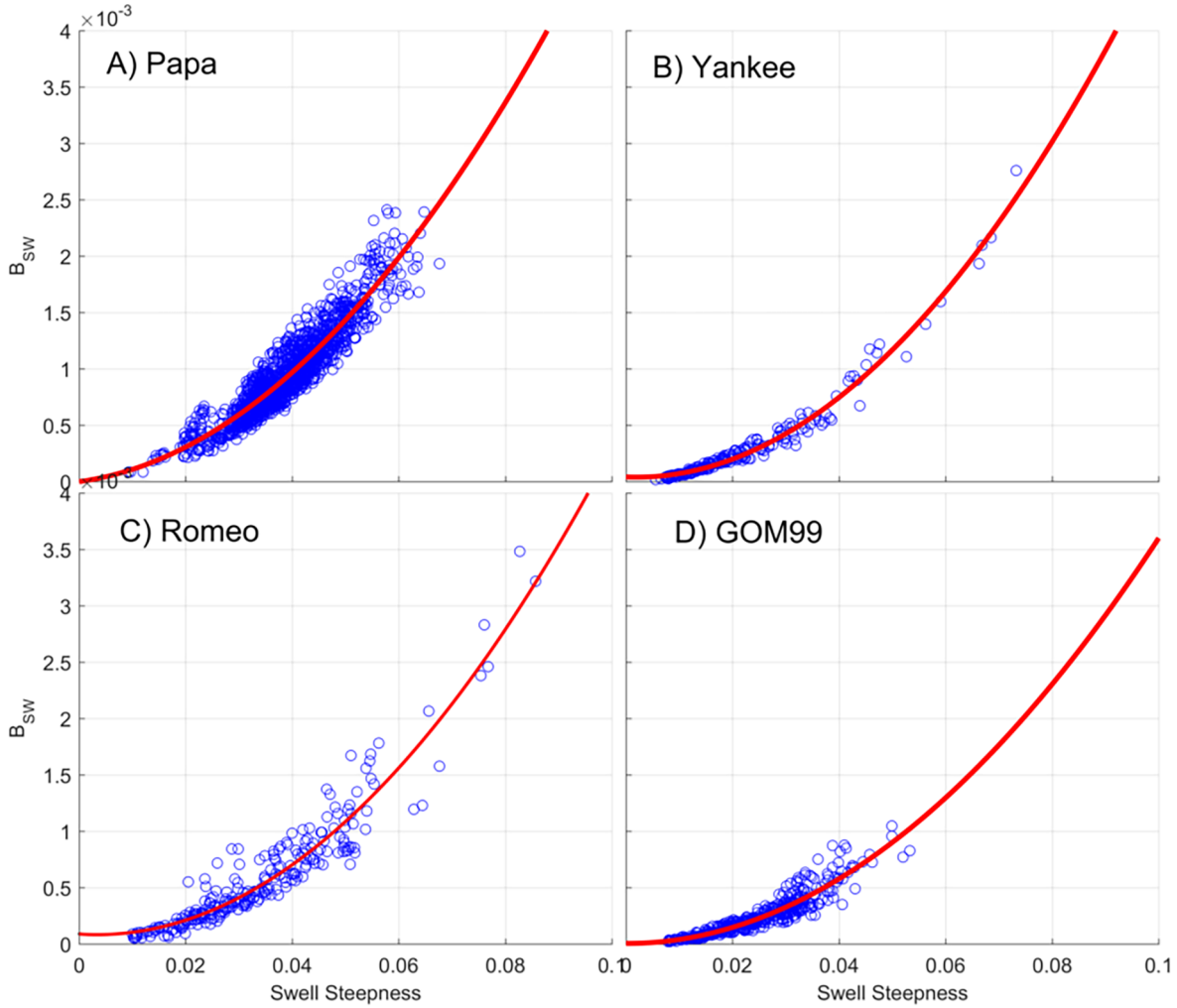

Fig. 24. Relationship between B_{sw} and swell steepness for cases R > 90 and U < 6 m/s for the four data sets. A quadratic fit to the data appears appropriate.

spectral tail which defines both the equilibrium and saturation range as a function of swell steepness and wind speed[a] is:

$$E(f) = \Phi(f) = B_4[\delta f^{-4} + (1-\delta) f_t f^{-5}] = B_4 \Phi_o(f) \tag{34}$$

with

$$\Phi_o(f) = [\delta f^{-4} + (1-\delta) f_t f^{-5}] \tag{35}$$

In the 'pure' wind-sea case Eq. (32) becomes

$$S_{ino}(U, f, \theta) = \Pi \times \cos(\theta - \theta_w) \times E(f) \times D(f, \theta) \tag{36}$$

$$= \Pi \times \cos(\theta - \theta_w) \times B_o \Phi_o \times D(f, \theta) \tag{37}$$

where B_o denotes the value of B_4 for U given no swell.

In a swell case we note that the form of Π does not change because we are still in the same high frequency range and at angles that our observations show only are in the wind-sea direction, presumably having the same local sheltering[b]. Therefore, the swell case input function becomes (using $B_4 = \lambda B_o$)

$$S_{inS}(U, f, \theta) = \Pi \times \cos(\theta - \theta_w) \times B_o \Phi_o \times D(f, \theta) \tag{38}$$

$$= \Pi \times \cos(\theta - \theta_w) \times \lambda B_o \Phi_o \times D(f, \theta) \tag{39}$$

$$= \lambda [\Pi \times \cos(\theta - \theta_w) \times B_o \Phi_o \times D(f, \theta)] \tag{40}$$

$$= \lambda S_{ino}(U, f, \theta) \tag{41}$$

where $\lambda = B_4/B_0$ represents the modulation due to swell. We estimate u_*^2 by

$$u_*^2 = \rho_w/\rho_a g \iint \frac{S_{in}(U, f, \theta)}{C(f)} d\theta df \tag{42}$$

with the integrals taken for all directions and for f > 0.33 Hz (hence ignoring contributions from longer waves). For a 'pure' wind-sea with velocity U

$$u_{*o}^2 = \rho_w/\rho_a g \iint \frac{S_{ino}(U, f, \theta)}{C(f)} d\theta df \tag{43}$$

Using Eq. (42), where swell is present,

$$u_{*S}^2 = \rho_w/\rho_a g \iint \frac{S_{inS}(U, f, \theta)}{C(f)} d\theta df \tag{44}$$

[a] We noted earlier that the power laws could be expressed either in wave number or frequency space and that our choice of frequency is because our spectra are frequency spectra. An equivalent to the analysis can be made in wave number space.

[b] The transition frequency f_t may be different in the swell versus the 'pure' sea case. If the winds are high, the case of high swell steepness or dominance is unlikely so there may be very little difference. In the case of low wind speed f_t is relatively high (at 4 m/s approximately 1 Hz). The effect of swell perhaps moves this to 0.7–0.8 Hz. At these frequencies the difference in the values of the power laws is small. Neglecting it may have a small impact for which we do not account.

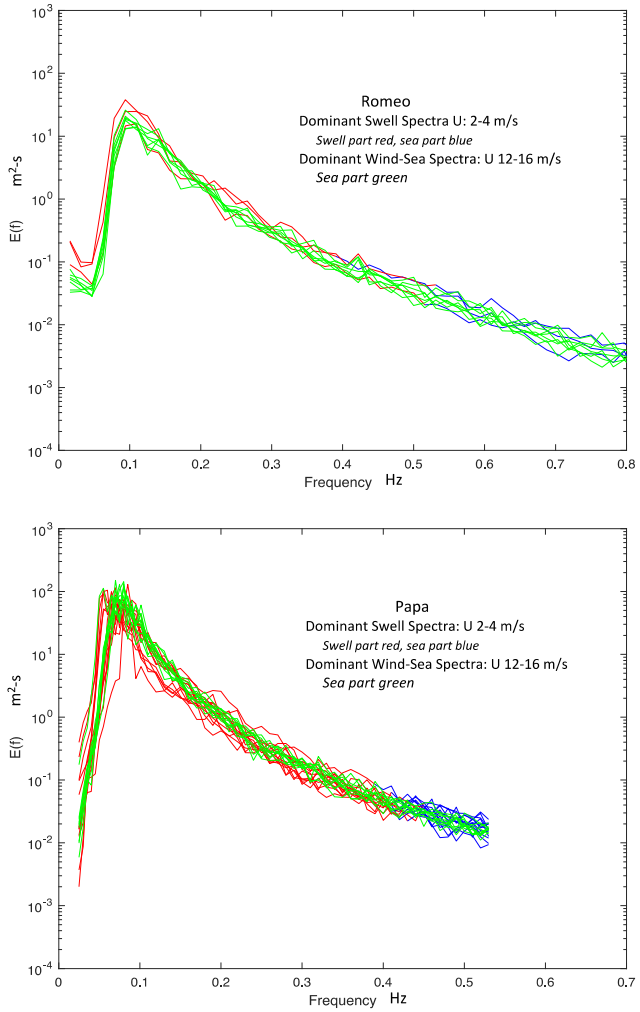

Fig. 25. Comparison of pure sea and swell spectra for Romeo and Papa. Wave conditions have wave heights of 4–6 m and peak frequencies 0.09–0.10 Hz. All spectra have very similar shapes, much like a typical wind sea whether sea or swell dominant.

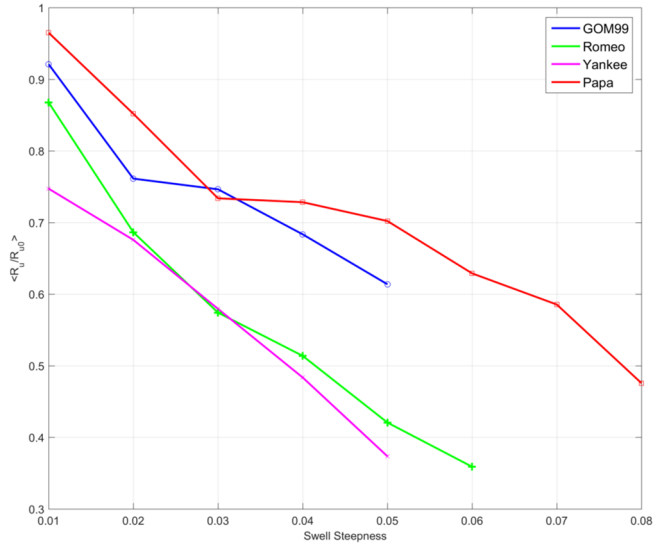

Fig. 26. Averages of the ratio of R_u/R_{u0} versus swell steepness. The trends indicates that as swell steepness increases the transition frequency is at a lower frequency than a pure wind sea at the same wind speed. The normalization factor $R_{u0\ 0}$ is specific to each buoy.

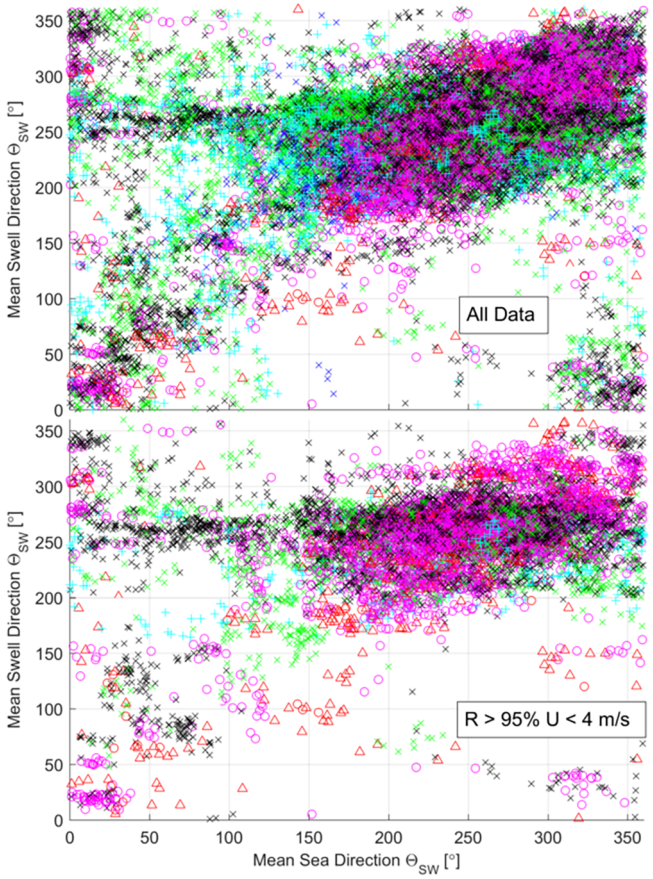

Fig. 27. Comparisons of sea (θ_{SE}) and swell (θ_{Sw}) directions at Papa. Top panel is for all data, bottom panel for cases with little sea (R > 95%) and low winds (U < 4 m/s). Directions are degrees true north. The steepness of each observation is color coded as follows: 0–0.01 blue x, 0.01–0.02 cyan +, 0.02–0.03 green x, 0.03–0.04 black x, 0.04–0.05 magenta o, and greater than 0.05 red o. (For interpretation of the references to color in this figure legend, the reader is referred to the web version of this article.)

$$= \rho_w/\rho_a g \iint \lambda \frac{S_{ino}(U,f,\theta)}{C(f)} d\theta df \tag{45}$$

$$= \lambda \rho_w/\rho_a g \iint \frac{S_{ino}(U,f,\theta)}{C(f)} d\theta df \tag{46}$$

$$= \lambda u_{*o}^2 \tag{47}$$

This equation is physically appealing: stress when swell is present is proportional to the modulation times what it would be absent swell. This estimate is based only on the tail and neglects the other parts of the spectrum, which may also contribute to the total stress.

We cannot calculate u_{*0} from first principles; however, we can develop an empirical form from our data sets much as Drennan et al. (1993) does for the drag coefficient. We note in an approach such as Donelan et al. (2012), the problems of the many unknown factors such as sheltering coefficients are resolved via a calibration as well. Here the empirical adjustment is directly evident and since we restrict the fit to 'pure wind-sea' cases any influence of swell has been removed.

We re-iterate our assumptions: we are looking only at the momentum transport in the high frequency tail, and that the directional function D is approximately the same in both cases above 0.33 Hz. The directional data from Papa indicate that when swell is present the mean direction of the tail remains in the wind direction. Whatever the process by which swell modulates the energy of the tail, the result leads to modulation of the energy in short waves associated with the wind direction. Most importantly it does not result in energy transfer into short

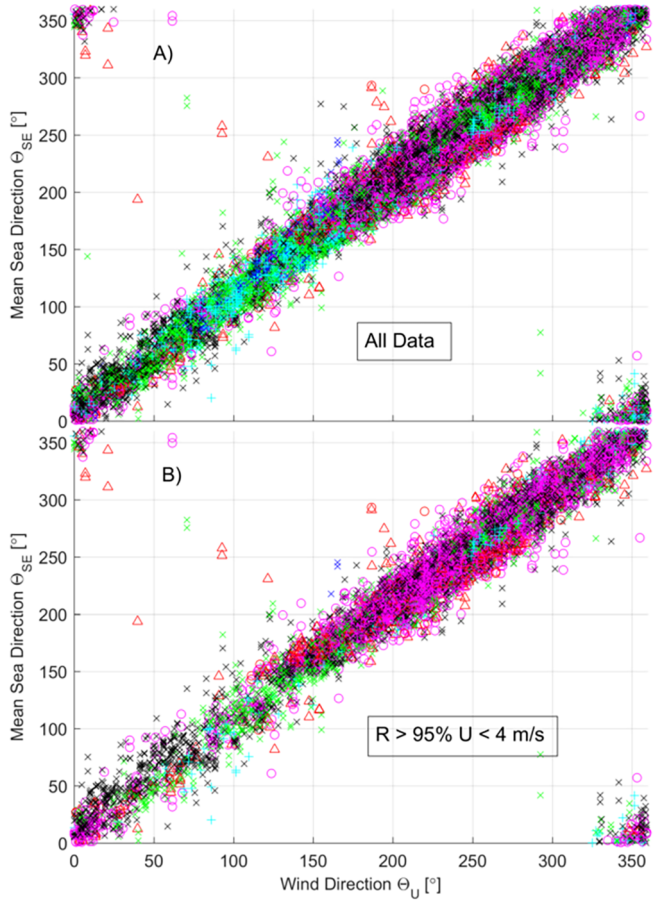

Fig. 28. Comparisons of sea (θ_{SE}) and wind directions (θ_W) for Papa. Top panel is for all data, bottom panel for cases with little sea (R > 95%) and low winds (U < 4 m/s). Directions are degrees true north. The steepness is color coded as In Fig. 27.The bottom panel shows that even in the case of nearly pure swell the high frequency wind sea tail is in the wind direction and within approximately ± 30 degrees. There is no obvious differentiation with steepness.

waves in the swell direction (excepting the case where sea and swell are co-linear) since mean wave direction aligns with the wind direction. We note that in the mid-part of the spectrum the wave angle can deviate from the wind direction.

4.3. Evaluation of the swell influenced stress equation

Our approximation is similar to traditional drag laws such as Wu (1982), Smith (1980), or Andreas et al. (2012) which predict the magnitude but not the direction of the stress. We have followed a formulation in terms of friction velocity as recommended by Andreas et al. (2012) because of its logic and because we can produce a similar result from GOM99 data set. The factor $\lambda^{1/2}$ is computed from the spectrum and applied to estimate the swell modulated friction velocity from the 'pure' wind-sea estimate:

$$u_{*S} = \lambda^{1/2} u_{*o} \tag{48}$$

with the $u_{*o} - U$ relationship is derived from data.

We evaluate Eq. (48) to see how much of the stress may be attributed the modulation of the spectral tail by the swell. The GOM99, and the SW06 experiment (Romeo and Yankee) buoys measured U, u_* and the wave spectrum from which B_4 has been estimated. u_* was not measured at Papa. In Fig. 13 we show the $B_o - U$ relationship and in Fig. 29 the $u_{*o} - U$ relationship for each buoy. At Yankee and Romeo, the $u_{*o} - U$ relationship is bi-linear with a split near 10 m/s. Andreas et al. (2012) show a similar pattern. It may well be that the strong boundary layer stability of much of the low wind data in SW'06 amplifies this break. As with the $B_o - U$ relationship, at very low wind speeds u_{*o} appears to go to zero while U is low but non-zero. We set u_{*o} to a low minimum value taking the view of Andreas et al. (2012) that this may be a smooth flow regime.

We calculate $\lambda = B_4/B_o$ from the spectral observations, compute u_{*o} from the measured U, estimate u_{*S}, and then compare it to the observed value u_*. The data from the three ASIS buoys allow comparison for winds up to 22 m/s for nearly 3000 cases including both stable and neutral conditions. Time synchronized plots (Fig. 30) of the predicted and observed values for the three buoys had correlations of 0.81–0.97. The grouped scatter plot (Fig. 31) shows a moderately high correlation (0.91) with the results roughly linear with the equation explaining about 83% of the variation. The best fit to the cross-plots has a slope of 0.83–0.86 suggesting our estimate is somewhat low above a u_* of 0.5 m/s, but at lowest wind speeds is slightly high.

Fig. 32-A is a plot of u_*/u_{*o} as a function U for cases with the highest range of swell steepness observed (> 0.04 for GOM99, Romeo and Yankee). The plot shows that the u_*/u_{*o} values are generally greater than 1 and at the lower wind speeds the ratio can be 3–6 suggesting significantly amplified drag. We also plot the values of $\lambda^{1/2}$against U for the same observations showing that in they follow a general trend of the u_*/u_{*o} curves but at the lowest wind speeds overestimate the u_*/u_{*o} trend. A clear and important difference is that u_*/u_{*o} has more scatter than $\lambda^{1/2}$. We also took the quadratic curve from Andreas et al. (2012) Eq. (27) to compute his estimate of u_* and normalize it by our estimate of u_{*o} from GOM99 since the stability was largely neutral for that data set and Andreas et al. uses an equivalent neutral 10 m wind speed. We note that there are not many examples with swell steepness much above 0.04 in these data sets.

The same analysis is performed for data subsets with between 0.02 and 0.03 (Fig. 32-B) and swell steepness less than 0.01 (Fig. 32-C). The curves for u_*/u_{*o} show a clear trend to be progressively higher as swell steepness increases. The $\lambda^{1/22}$ curve follows the same trends still somewhat higher than the u_*/u_{*o}curve. Swell steepness in our data sets had a mean in the 0.02–0.04 range which may be typical of general ocean sea states. That the normalized Andreas et al. curve appears to curve upward in the mid swell steepness range suggests that its values at lower winds may be due the swell influence. Since it is a best fit to data, the swell influence has likely been calibrated into the curve.

The conclusion is that u_*/u_{*o} has a steepness related component and that the $\lambda^{1/2}$ approach follows a similar trend but may be high at the lowest wind speeds. The larger variation in u_*/u_{*o} at a given wind speed than $\lambda^{1/2}$ may be physically significant rather than just random errors. We neglected the role of the direct impact of the swell at low frequencies in order to understand what the impact of the swell induced modulation may be. Estimates of B_o and u_{*o} can introduce error. Moreover, at very low wind speeds with steep, large swell much of the wind may be driven by the swell and has a jet-like structure atypical of normal wind driven situation. It may be that when the swell is very steep, there is a limit on the rate or amount of momentum transported downwards because of the shallow nature of the wind jet. One can conceive of a situation where the estimated input taken from the jet (which is based on a typical deep boundary layer theory) could significantly damp the jet. However, we also note that the momentum transport in the tail is downward while the part in the swell frequencies, neglected, is upward which may correct part of the overprediction via $\lambda^{1/2}$.

We compared predictions from Eq. (45) to that of Andreas et al. for the three data sets. For GOMEX99, where the atmosphere is normally neutral, the trends in the Eq. (45) versus Andreas et al. scatter plot were very similar (linear coefficient of 0.83 versus 0.81, constant 0.051 versus 0.019), but Andreas et al had a better correlation 0.94 versus 0.87. Correlation for the entire data set was the reverse 0.87 for Andreas et al. versus 0.91 for Eq. (45). Our conclusion is that Andreas et al. likely provides a better answer (based on the neutral stability cases) than Eq. (45) possibly because the effect of swell has been calibrated into it. However, Eq. (45) provides almost as good an answer while sensitive to the apparent effect of swell. We conclude that the modulation of the roughness by the swell appears to be a significant factor that should be considered.

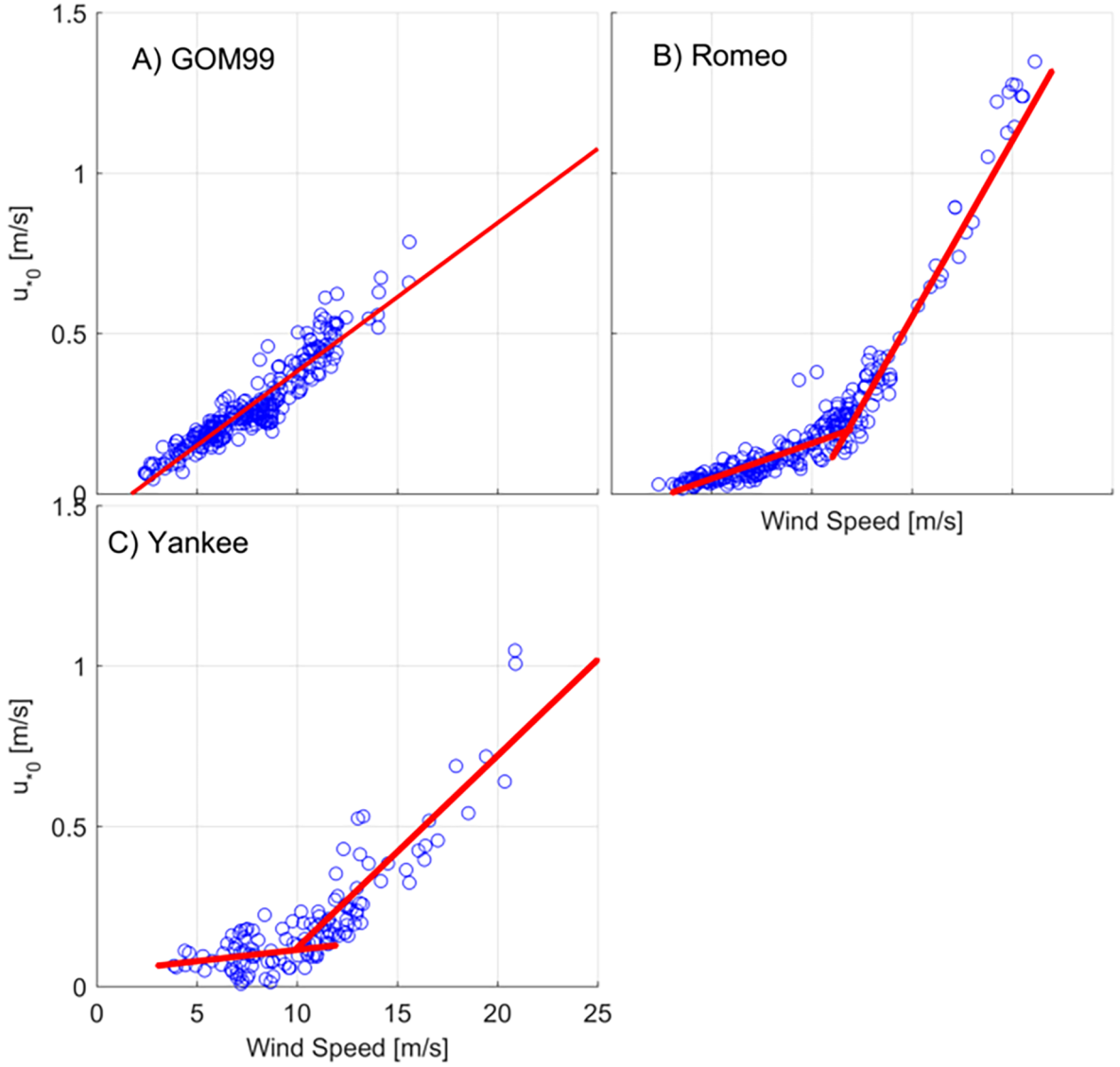

Fig. 29. Plot of the friction velocity for pure wind-sea cases u_{*0} against Wind speed. Pure wind-sea cases defined by swell steepness less than 0.015. The need for 2 linear functions for Yankee and Romeo is believed due to the many cases of highly stable atmospheric stability at lower wind speeds. There is a slight inflection in GOM99 about 8 m/s as indicated by Andreas et al. but compared to Yankee and Romeo it is almost linear. Friction velocity was not measured at Papa.

4.4. Swell-generated winds

We consider the Harris (1966) case: no large-scale atmospheric pressure forcing of the surface wind, with large, steep swell generating a wind near the surface, but not high into the atmosphere. The pure-swell cases with low wind-speeds discussed earlier may contain cases like this. Driven by the large momentum flux correlated with the swell peak, we would expect the swell would generate a mean wind in the lower atmosphere with a jet maximum potentially as high as 8–10 m above the surface. Although the wind is generated by the swell, it is still a wind, though perhaps weak, with a boundary layer (Högström et al., 2013; Jiang et al., 2016). Small, short waves should grow filling energy into what is a wind-sea tail. Swell fields are typically coherent over large areas allowing ample time and fetch for these waves to grow. Since the wind is driven by the swell, its direction will be in the direction of swell movement. Theoretically we would expect a small wind-sea spectrum to develop on the tail of the swell spectrum.

The Harris situation differs from a 'pure' wind-sea at the same low wind speed because the energy in the lower frequencies is dominated by a large, steep swell, rather than a low wind-sea consistent with a low swell-driven wind speed. As a consequence, the 4-wave interaction source term S_{nl} would be dominated by the swell with an energy flux much larger than it would be if the wind was really low and no swell present. As suggested in Section 3.3, the nonlinear source term can be equivalent to that of a wind-sea with a wind 12–16 m/s for very large swell.

Examining the Romeo data set for cases with steep, large swell at low wind speeds to match cases to low wind speeds and minimum swell finds two cases (Fig. 33). Case A contains the large swell spectra (swell height 4–6 m) at low wind speeds (2–4 m/s). Case B has spectra with minimum swell at similar wind speeds to Case A. Comparing Case A and B, it is clear that given the same low wind speed range, the energy in the wind-sea high frequencies in the large swell case is significantly higher (about a factor of 10) than those with minimal swell. Looking at all four data sets it is not possible to find 'pure' wind-seas at very low wind speeds, so the tails of the Case B spectra might actually be elevated above the 'pure' wind-sea case. In Fig. 34 we match a large swell (4–5 m), low wind (2–4 m/s) case from Romeo with a low wind (5–6 m/s), low swell case from GOM99 to better understand the possible differences with a 'pure' wind-sea spectrum. The energy in the tail in the swell case is still greater than that in the wind-sea even though the wind speed is nearly twice as high as the original comparisons for Case A.

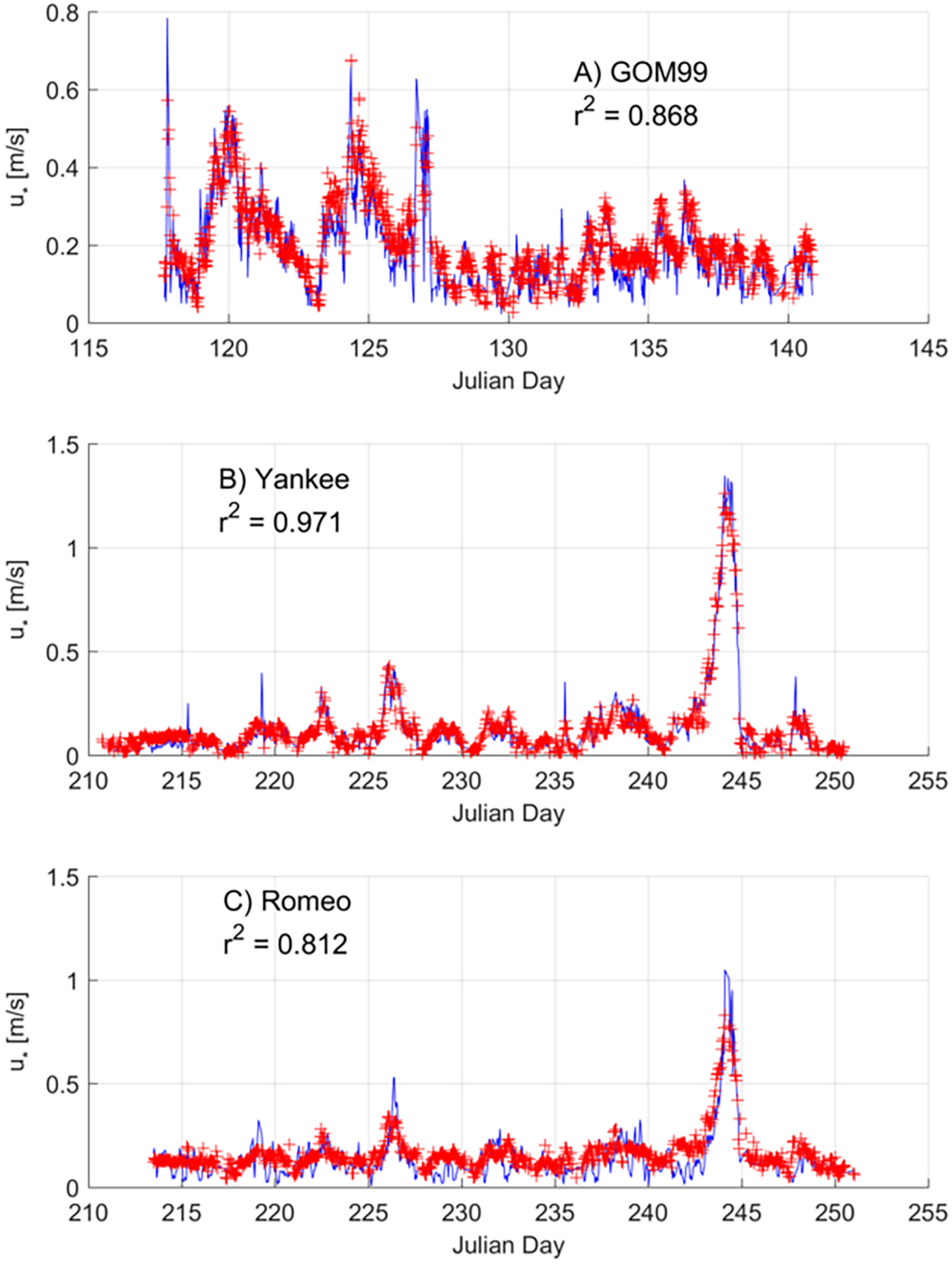

Fig. 30. Time plot of predicted versus observed friction velocity over time for three experiments. Observed value is the blue line, prediction red +. (For interpretation of the references to color in this figure legend, the reader is referred to the web version of this article.)

The equation for S_{nl} by Hasselmann and Hasselmann (1985)

$$S_{nl}(f, \Theta) = g^{-4} E_t^3 f_p^8 D_{nl}\left(\frac{f}{f_p}, \Theta\right) \tag{49}$$

where D_{nl} is a dimensionless shape function, dependent on the shape of the spectrum but not E_t, may be used to estimate the differences for Cases A and B. For Romeo the swell has wave heights of 4–6 m with peak frequency near 0.1 Hz when the winds are 2–4 m/s. The wind-sea in the low swell cases is at a peak frequency of about 0.45 Hz and has a height of about 0.5 m. Calculating the total energies of based on 6 m versus 0.5 m and for peak frequencies 0.1 versus 0.45 Hz the ratio of the two S_{nl}'s is $[E_t^3 f_p^8]_{swell}/[E_t^3 f_p^8]_{wind-sea} \cong 17.8$. The theory supports a significantly larger energy flow from the peak of the swell than that of the 'pure' wind-sea peak.

The data support the notional concept: (1) a wave-driven wind develops from the propagation of the steep swell, (2) the positive, upward momentum transfer generates a low speed, shallow wind which causes short wind-waves and the beginnings of a wind-sea tail, (3) at

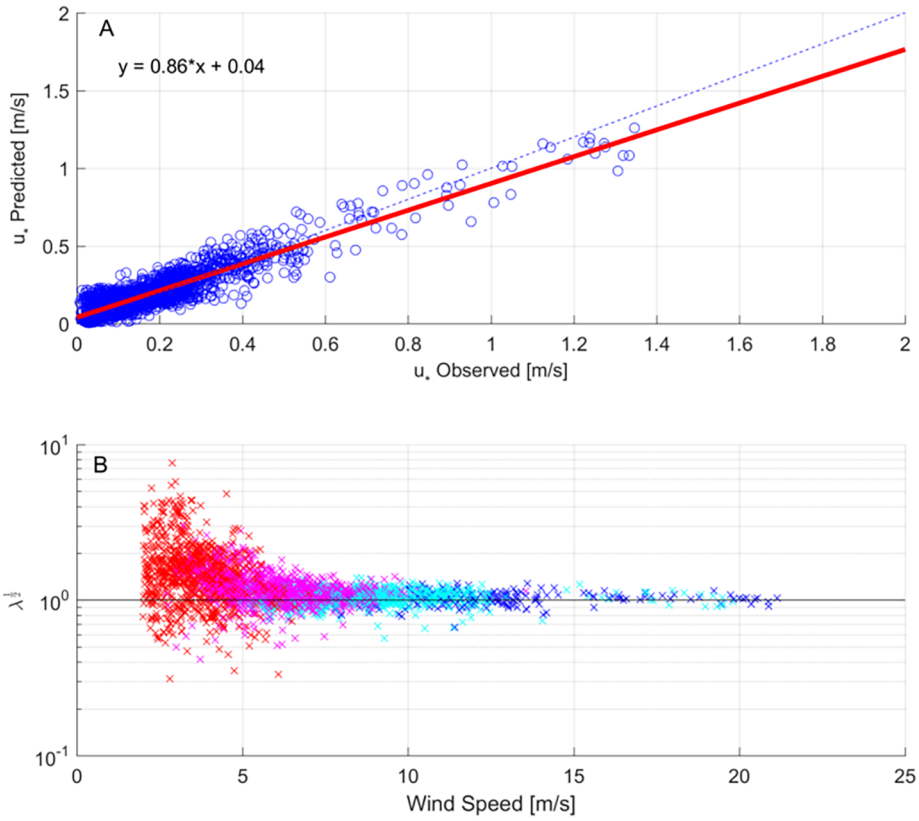

Fig. 31. Prediction of friction velocity (u_*) and $\lambda^{1/2}$ for GOM99, Yankee and Romeo data sets. Panel (A) shows observed versus predicted friction velocity. u_{*0} and B_0 are estimated from the relation with U. The red line is the best fit, the blue line is a l: 1 fit. Panel (B) provides calculated values of $\lambda^{1/2}$ from the observed B_4 and estimated B_0. Swell percentage R of 0–10% is colored in blue, 10–50% in cyan, 50–90% in magenta, and more than 90% in red. Impact of swell ($\lambda^{1/2}$) appears to be greatest at lower wind speeds and highest amounts of swell. (For interpretation of the references to color in this figure legend, the reader is referred to the web version of this article.)

the same time the swell drives a flux of energy into the tail due to S_{nl} amplifying the energy level of the tail and in the direction of the swell which is the wave-driven wind direction, and (4) results in additional stress due to the short-waves in the tail. This extra stress is due to the swell part of the spectrum, but it is via modulation of the shorter waves most likely via S_{nl}. The result would be apparently larger drag than if no swell were present. But this is theoretical conjecture.

4.5. Discussion concerning swell modulation of stress

Our analyses suggested that the swell modulated tail would explain about 80% of the variance of the stress in the prediction comparison sets and that u_* is overpredicted at the lowest wind speeds, slightly underpredicted at the higher speeds. The total stress due to the swell $[u_*^2]_{sw}$ should be a combination the direct action of the swell $[u_*^2]_{swd}$ and the indirect portion from the tail $[u_*^2]_{hfs}$, suggesting that $[u_*^2]_{hf}$ should be decomposed into a swell modulated part $[u_*^2]_{hfs}$ and a wind-input part $[u_*^2]_{hfw}$. Future allocation of the source of the stress needs to consider these partitions. A limitation of this paper is that $[u_*^2]_{swd}$ was not considered and that previous studies have not considered $[u_*^2]_{hfs}$.

The stress problem is perhaps easiest to understand at the extremes of swell dominance and pure-sea dominance. The general case becomes complicated: the swell may have separate peaks with waves traveling at different directions to the wind. If the amplification of energy in the tail is due to S_{nl}, it becomes strongly a function of the directional spectrum. Estimation via a practical forecast model would be expensive computationally if a sophisticated S_{nl} routine is used. A positive outcome from the study is the understanding that Eq. (45) may provide a swell sensitive approximation for u_* (noting its deficiencies) that future research may correct either empirically or by including the long wave components.

5. Conclusions and summary

5.1. Conclusions

The research reported had the overarching goal of understanding how the presence of swell might alter the wind-sea spectrum and aspects of air-sea interaction related to the wave spectrum. Two main questions were investigated: (1) *Can the modulation of the wind-sea spectral tail that happens when swell is present be represented by some modification of the power law formulation* Φ *of the spectral tail and its parameters, and (2) Does the modulation of the spectral tail significantly alter the stress.*

The results reported in Section 3 of the paper clearly support a conclusion that swell can significantly impact the equilibrium and saturation range of the wind-sea and that this can represented through an enhancement of the tail as expressed in the function Φ through modification of its parameters [B_4, B_5, f_t] to account for the presence of swell.

We have established the relationships between [B_4, B_5, f_t] and wind speed for a 'pure' wind-sea and then shown that their values in the presence of swell is related to swell steepness noting that the effect appears largest at low wind speeds. The modification of B_4 as an example is represented by a factor $\lambda = B_4/B_o$ where B_o is the 'pure' wind-sea value of B_4 and λ is a function of swell steepness and wind speed. The relationships found were consistent over all the buoys representing a wide range of wind and wave conditions and it may be possible in the future to consolidate the parameters found into a universal parameterization for the spectral tail for conditions from 'pure' wind-sea through hybrid sea-swell mixtures to 'pure' swell. Analysis of 'pure' wind-sea and swell spectra of same height and peak frequency show that they appear equivalent and that in the swell case the tail is similar in magnitude to the wind-sea spectra. This in turn suggests that the nonlinear source term may be responsible for modulating the tail of the spectra.

The results of Section 4 show that a simple bulk formula relating

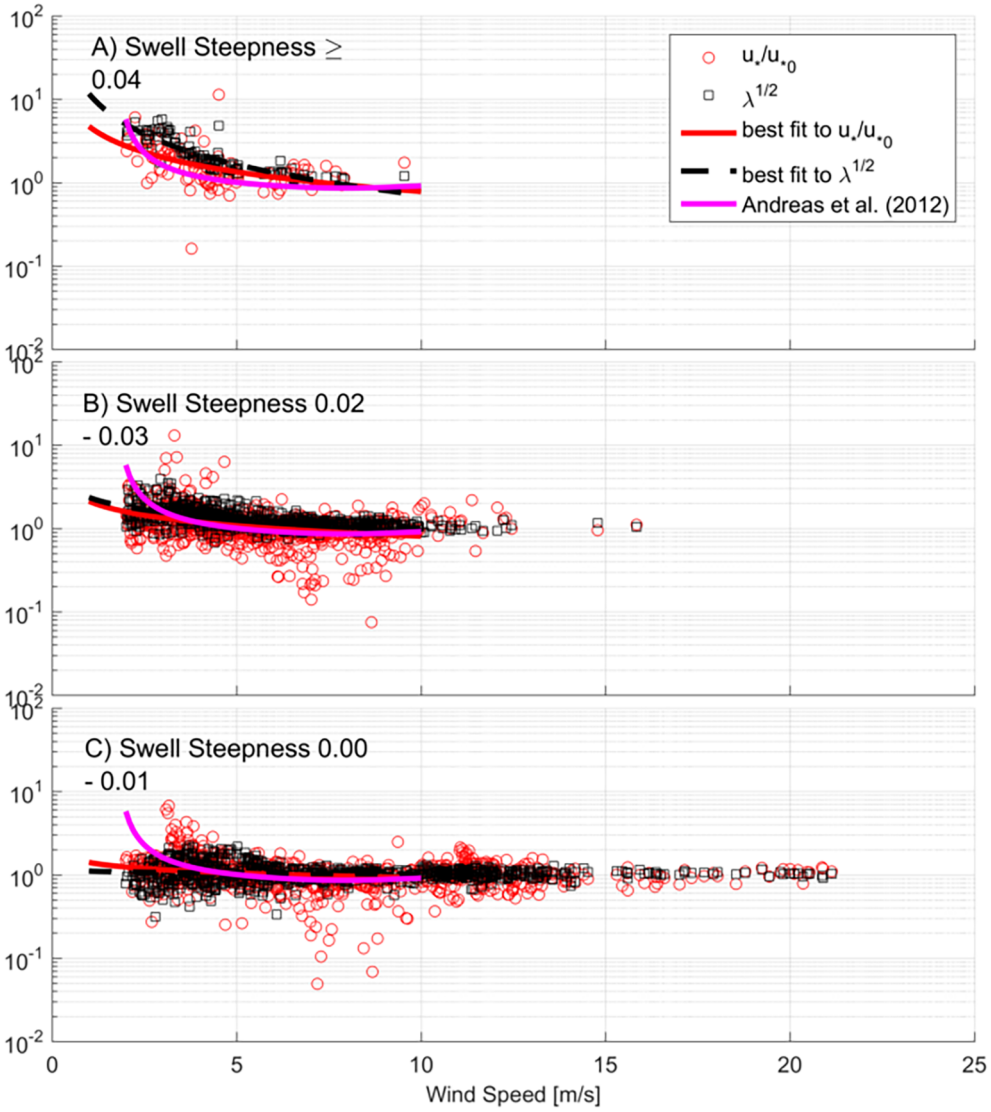

Fig. 32. Plots of u_*/u_{*0} and $\lambda^{1/2}$ versus wind speed U by different swell steepness ranges. Red circles are u_*/u_{*0} data points. Black squares are $\lambda^{1/2}$ data points. Red line best fit to u_*/u_{*0} points. Dashed black line best fit to $\lambda^{1/2}$ points. Magenta line normalized Andreas et al. (2012) prediction. The blue-green line is a constant of 1. (For interpretation of the references to color in this figure legend, the reader is referred to the web version of this article.)

stress with swell to that without can be developed from Donelan et al.'s (2012) approach simplified to only represent stress related to the high frequency tail. Evaluation of this equation with observations show that it predicts stress nearly as well as Andreas et al. (2012) while showing skill in estimating cases with significant amounts of swell. Analysis of u_*/u_{*0} show a dependence on swell and windspeed similar to $\lambda^{1/2}$. The results show that the equation may overestimate the stress at the very lowest wind speed and this is suggested to arise because the momentum transport in the swell frequencies is absent, a choice made to isolate the high frequency effect. The results suggest that future studies should include both swell effects. Analysis of the case of a swell generated wind suggests a framework by which the upward transport of momentum by the swell that generates a shallow local wind which in turn develops short waves in the high frequencies which are modulated by the swell. The consequence is a stress level higher than would be expected for just the swell generated local wind. The results of Section 4 clearly support a conclusion that the swell can have a significant impact on stress and that to properly represent it both swell effects (in the swell frequencies and via modulation of the spectral tail) should be included.

We hope our results will open up a new interest in how the entire wave spectrum responds to the differing combinations of sea and swell, however defined, and in particular when the entire spectrum must be considered coupled, not just the sum of sea and swell waves treated independently. Our observations are older and we would hope that better ones with more sophisticated instruments can be obtained. We feel that having a very large sample base across a wide range of conditions and environments is desirable. Among the important questions arising from the study is the dependence of the saturation zone on wind speed presumably before full saturation happens. What is the balance of source terms, are any missing, and why is the transition so abrupt. A second set of questions arises around the presence of the equivalents of the saturation and equilibrium ranges in pure swell. Do we really understand what produces the power laws? In terms of the stress formulation, the key questions arise around the relative influence of swell versus the wind sea. How does the swell generated upward flux affect the downward flux as the sea energy becomes larger than the swell (and vice versa)? How is this influenced by the interaction space of the wave-wave interactions which becomes sensitive to numbers and locations of wave systems in wave number space? Many of these questions might be resolved by either numerical simulation of the Boltzmann Integral (both phased averaged and phase resolving) and increases the need for simulations in which the waves and wind are actually fully coupled with

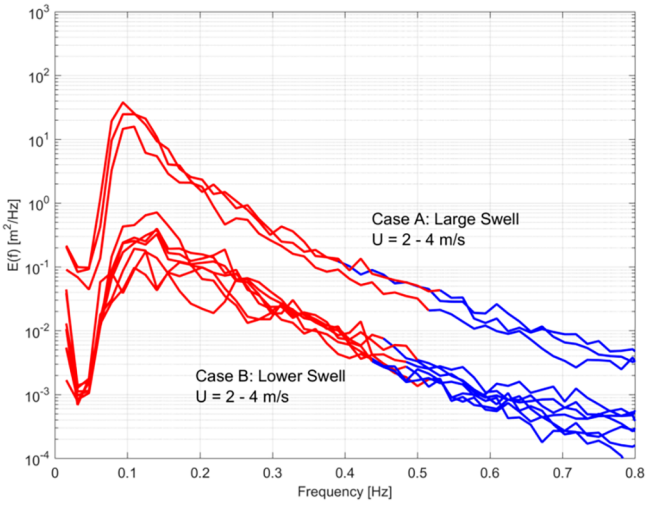

Fig. 33. Large versus small swell height conditions at low wind speed (2–4 m/s) at Romeo. Swell frequencies are in red, sea in blue. Case A significant wave height 4–6 m. Case B significant wave height approximately 0.5 m. (For interpretation of the references to color in this figure legend, the reader is referred to the web version of this article.)

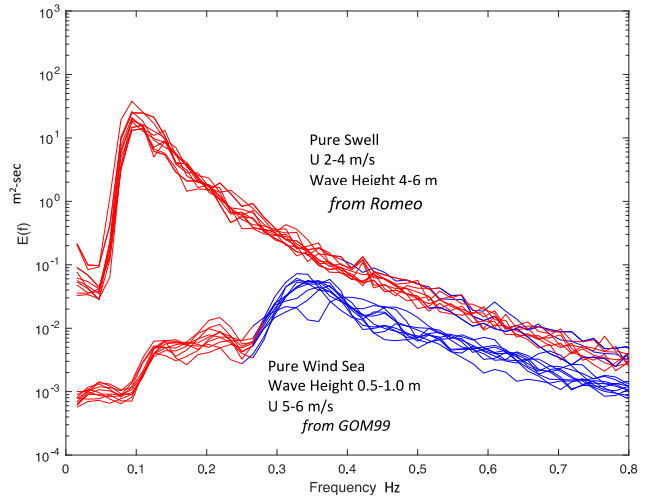

Fig. 34. Pure swell and sea spectra. Swell spectra from Romeo. The wind speed spectra are from GOM99 and represent the lowest pure wind sea data set of the four buoys. Measured u_* in pure sea cases 0.08–0.011 m/s, 0.18–0.22 m/s in swell case. Cases are drawn from ASIS buoys because of length of frequency domain to 0.8 Hz and under the assumption the cases are representative of these conditions anywhere.

breaking more realistically included. Finally, why does the wind sea peak decrease as the amount of swell present increases.

5.2. Summary

Observations indicate that swell modulates the energy levels of the equilibrium and saturation ranges but does alter not the power law formulation nor the mean wave direction. Since these sub-ranges were initially proposed only for wind-seas and are often explained in terms of balances of wind input, breaking and nonlinear energy transfers within the wave field, their existence in 'pure' swell suggests that S_{nl} may be the dominant factor as suggested by Kitaigorodskii (1983) controlling the equilibrium range.

The values of the spectral sub-range coefficients B_4 and B_5 and the transition frequency f_t for the power laws are estimated. Their relationship to wind speed and factors of the wave field such as swell steepness is statistically determined. The data show that the description of the spectral tail by the function Φ may be generalized to hybrid sea-swell cases. The observations show that B_4 and B_5 are a function of swell steepness and wind speed. Scatter remains suggesting that factors beyond swell steepness may influence the interaction. The transition frequency between the equilibrium and saturation ranges agree with Lenain and Melville (2017) for wind-seas but the data shows that the presence of swell tends to shift the transition point towards lower frequencies. The data from the Ocean Station Papa buoy overwhelming showed that no matter the swell steepness, angle or dominance, the mean direction of the high frequency tail of the spectrum is that of the wind.

The impact of swell on transfer of momentum between the air and ocean in the tail of the spectrum is calculated by neglecting the contributions from lower swell frequencies. This yields a simple formula $u_* = \lambda^{1/2} u_{*o}$. Data from the Gulf of Mexico and SW06 experiment indicate that the modulation effect explains about 80% of the variance in the prediction-observation comparisons. Observed u_*/u_{*o} exhibit a positive trend with steepness as does the factor $\lambda^{1/2}$. However, $\lambda^{1/2}$ overestimates u_*/u_{*o} at very low wind speeds suggesting that adding in an adjustment related to the low frequency swell components should be of value. The momentum transport in the tail is downward while the transport in the swell frequencies is upward. The new equation appears almost as good as that of Andreas et al. but importantly incorporates a sensitivity to swell steepness that Andreas et al. does not.

The wave-driven wind case of Harris (1956) is considered theoretically and via observations. Swell would drive an upward flux of horizontal momentum in its direction producing a wind that generates a low energy spectral tail in the swell (and hence wind) direction. At the same time the S_{nl} nonlinear interactions driven by the large, steep swell pump significant additional energy into the tail promoting additional surface roughness and stress. The total stress must combine the upward and downward components. Compared to the same wind speed without swell, the stress would appear greater than expected. Extension of these concepts to the general case complex due to the role of S_{nl} which would be sensitive to spectral morphology that can be complicated by multiple wave systems. Further theoretical analyses and use of more modern data sets are required to evaluate these concepts more fully. It may be plausibly argued that once swell becomes sufficiently steep the entire wave system should be considered as a coupled unit which also mediates air-sea interaction.

Acknowledgements

The authors acknowledge the Office of Naval Research and the National Science Foundation for the support of the original data collection and analysis studies and for the investigators who maintained and shared the data sets. At Papa the efforts of Joe Talbert and Alex de Klerk for mooring design and support and the California Data Collection Program for data telemetry and archiving is acknowledged. Support for research at the University of Miami was from the Office of Naval Research and the Marine Meteorology Division of the Naval Research Laboratory via the University Consortium for Atmospheric Research. Support for the Applied Physics Laboratory was provided by the National Science Foundation. Research at the Field Research Facility was supported by the US Army Corps of Engineers.

References

Alves, J., Banner, M., Young, I., 2003. Revisiting the pierson-moskowitz asymptotic limits for fully developed wind waves. J. Phys. Oceanogr. 33, 1301–1323. https://doi.org/10.1175/1520-0485(2003)033>3C1301:RTPALF>3E2.0.CO;2.

Andreas, E.L., Mahrt, L., Vickers, D., 2012. A new drag relation for aerodynamically rough flow over the ocean. J. Atmos. Sci. 69, 2520–2537. https://doi.org/10.1175/JAS-D-11-0312.1.

Ardhuin, F., Chapron, B., Collard, F., 2009. Observation of swell dissipation across oceans. Geophys. Res. Lett. 36https://doi.org/10.1029/2008GL037030. L06607.

Ardhuin, F., Rogers, E., Babanin, A.V., Filipot, J.-F., Magne, R., Roland, A., van der Westhuysen, A., Queffeulou, P., Lefevre, J.-M., Aouf, L., Collard, F., 2010. Semi-empirical dissipation source functions for ocean waves. Part I: definition, calibration, and validation. J. Phys. Oceanogr. 40, 1917–1941. https://doi.org/10.1175/2010JPO4324.1.

Ardhuin, F., Roland, A., Dumas, F., Bennis, A.-C., Sentchev, A., Forget, P., Wolf, J., Girard, F., Osuna, P., Benoit, M., 2012. Numerical wave modeling in conditions with strong currents: dissipation, refraction, and relative wind. J. Phys. Oceanogr. 42, 2101–2120. https://doi.org/10.1175/JPO-D-11-0220.1.

Banner, M.L., 1990. Equilibrium spectra of wind waves. J. Phys. Oceanogr. 20, 966–984. https://doi.org/10.1175/1520-0485(1990)020<0966:ESOWW>2.0.CO;2.

Chen, G., Chapron, B., Ezraty, R., Vandemark, D., 2002. A global view of swell and wind-sea climate in the ocean by satellite altimetry and scatterometry. J. Atmos. Oceanic Technol. 19, 1849–1859. https://doi.org/10.1175/1520-0426(2002)019<1849:AGVOSA>2.0.CO;2.

Collins III, C., 2012. In situ wave measurements: Sensor comparison and data analysis. University of Miami. Open Access Theses, (Paper 372) (Open Access).

Collins III, C., Potter, H., Lund, B., Tamura, H., Graber, H., 2018. Directional wave spectra observed during intense tropical cyclones. J. Geophys. Res. (Oceans). https://doi.org/10.1002/2017JC012943.

Donelan, M., Hamilton, J., Hui, W.H., 1985. Directional spectra of wind-generated waves. Philos. Trans. R. Soc. Lond. 315A, 509–562. https://doi.org/10.1098/rsta.1985.0054.

Donelan, M., Drennan, W., Katsaros, K., 1997. The air-sea momentum flux in conditions of wind-sea and swell. J. Phys. Oceanogr. 27, 2087–2099. https://doi.org/10.1175/1520-0485(1997)027<2087:TASMFI>2.0.CO;2.

Donelan, M., Curcic, M., Chen, S., Magnusson, A., 2012. Modeling waves and wind stress. J. Geophys. Res. 117, C00J23. https://doi.org/10.1029/2011JC007787.

Drennan, W., Graber, H., Donelan, M., 1999. Evidence for the effects of swell and unsteady winds on marine wind stress. J. Phys. Oceanogr. 29, 1853–1864. https://doi.org/10.1175/1520-0485(1999)029<1853:EFTEOS>2.0.CO;2.

Drennan, W., Graber, H., Hauser, D., Quentin, C., 1993. On the wave age dependence of wind stress over 'pure' wind-seas. J. Geophys. Res. 108 (C3). https://doi.org/10.1029/2000JC000715.

Forristall, G., 1981. Measurements of a saturated range in ocean wave spectra. J. Geophys. Res. 86, 8075–8084. https://doi.org/10.1029/JC086iC09p08075.

García-Nava, H., Ocampo-Torres, F., Hwang, P., Osuna, P., 2012. Reduction of wind stress due to swell at high wind conditions. J. Geophys. Res. 117, C00J11. https://doi.org/10.1029/2011JC007833.

Garcıa-Nava, H., Ocampo-Torres, F., Osuna, P., Donelan, M., 2009. Wind stress in the presence of swell under moderate to strong wind conditions. J. Geophys. Res. 114, C12008. https://doi.org/10.1029/2009JC005389.

Graber, H., Terray, E., Donelan, M., Drennan, D., Van Leer, J., Peters, D., 1999. ASIS—a new air-sea interaction spar buoy: design and performance at sea. J. Atmos. Oceanic Technol. 17, 708–720. https://doi.org/10.1175/1520-0426(2000)017<0708:AANASI>2.0.CO;2.

Grachev, A., Fairall, C., 2001. Upward momentum transfer in the marine boundary layer. J. Phys. Oceanogr. 31, 1698–1711. https://doi.org/10.1175/1520-0485(2001)031<1698:UMTITM>2.0.CO;2.

Grare, L., Lenain, L., Melville, W., 2013. Wave-coherent airflow and critical layers over ocean waves. J. Phys. Oceanogr. 43, 2156–2172. https://doi.org/10.1175/JPO-D-13-056.1.

Hanley, K., Belcher, S., Sullivan, P., 2010. A global climatology of wind–wave interaction. J. Phys. Oceanogr. 40 (6), 1263–1282. https://doi.org/10.1175/2010JPO4377.1.

Harris, D., 1966. The wave-driven wind. J. Atmos. Sci. 23 (6), 688–693. https://doi.org/10.1175/1520-0469(1966)023<0688:TWDW>2.0.CO;2.

Hasselmann, K., et al., 1973. Measurements of wind-wave growth and swell decay during the Joint North Sea Wave Project (JONSWAP). Deutsche Hydrographische Zeitschrift 8, 1–95.

Hasselmann, K., 1962. On the non-linear energy transfer in a gravity-wave spectrum. 1: General theory. J. Fluid Mech. 12, 481. https://doi.org/10.1017/S0022112062000373.

Hasselmann, K., 1963. On the non-linear energy transfer in a graviy-wave spectrum, Part 3; Evaluation of the energy flux and swell-sea interaction for a Neumann spectrum. J. Fluid Mech. 5, 385–398. https://doi.org/10.1017/S002211206300032Xj.

Hasselmann, S., Hasselmann, K., 1985. Computations and parameterizations of the non-linear energy transfer in a gravity-wave spectrum. Part I: A new method for efficient computations of the exact nonlinear transfer integral. J. Phys. Oceanogr. 15 (11), 1369–1377. https://doi.org/10.1175/1520-0485(1985)015<1369:CAPOTN>2.0.CO;2.

Högström, U., Rutgersson, A., Sahlée, E., Smedman, A., Hristov, T., Drennan, W., Kahma, K., 2013. Air-sea interaction features in the baltic sea and at a pacific trade-wind site: An inter-comparison study. Boundary Layer Meteorology 147 (1), 139–163. https://doi.org/10.1007/s10546-012-9776-8.

Högström, Ulf, Sahlée, Erik, Smedman, Ann-Sofi, Rutgersson, Anna, Nilsson, Erik, Kahma, Kimmo K., Drennan, William M., 2015. Surface stress over the ocean in swell-dominated conditions during moderate winds. J. Atmos. Sci. 72 (12), 4777–4795. https://doi.org/10.1175/JAS-D-15-0139.1.

Högström, U., Sahlée, E., Smedman, A., Rutgersson, A., Nilsson, E., 2018. The transition from downward to upward air–sea momentum flux in swell-dominated light wind conditions. J. Atmos. Sci. 75 (8), 2579–2588. https://doi.org/10.1175/JAS-D-17-0334.1.

Jiang, Q., Sullivan, P., Wang, S., Doyle, J., Vincent, L., 2016. Impact of swell on air-sea momentum flux and marine boundary layer under low-wind conditions. J. Atmos. Sci. 73, 2683–2697. https://doi.org/10.1175/JAS-D-15-0200.1.

Kahma, K., Donelan, M., Drennan, W., Terray, E., 2016. Evidence of Energy and Momentum Flux from Swell to Wind. J. Phys. Oceanogr. 46, 2143–2156. https://doi.org/10.1175/JPQ-D-15-0213.l.

Kitaigorodskii, S., Krasitskii, V., Zaslavskii, M., 1975. On Phillips' theory of equilibrium range in the spectra of wind-generated gravity waves. J. Phys. Oceanogr. 5, 410–420. https://doi.org/10.1175/1520-0485(1975)005<0410: OPTOER>2.0.CO;2.

Kitaigorodskii, S., 1983. On the theory of the equilibrium range in the spectrum of wind-generated gravity waves. J. Phys. Oceanogr. 13 (5), 816–827. https://doi.org/10.1175/1520-0485(1983)013<0816:OTTOTE>2.0.CO;2.

Kudryavtsev, V., Makin, V., 2004. Impact of swell on the marine atmospheric boundary layer. J. Phys. Oceanogr. 34, 934–949. https://doi.org/10.1175/1520-0485(2004)034<0934:IOSOTM>2.0.CO;2.

Lenain, L., Melville, K., 2017. Measurements of the directional spectrum across the equilibrium-saturation ranges of wind-generated surface waves. J. Phys. Oceanogr. 47, 2133–2138. https://doi.org/10.1175/JPO-D-17-0017.1.

Long, C., Resio, D., 2007. Wind wave spectral observations in Currituck sound, North Carolina. J. Geophys. Res. Oceans 112 (C5). https://doi.org/10.1029/2006JC003835.

Miles, J., 1957. On the Generation of surface waves by shear flows. J. Fluid Mech. 3 (2), 185–204. https://doi.org/10.1017/S0022112057000567.

Miller, H., Vincent, C., 1990. FRF spectrum: TMA with kitaigorodskii's f^{-4} scaling. J. Waterw. Port Coastal Ocean Eng. 116 (1), 57–78. https://doi.org/10.1061/(ASCE)0733-950X(1990)116:1(57).

Pan, J., Wang, D.W., Hwang, P., 2005. A study of wave effects on wind stress over the ocean in a fetch-limited case. J. Geophys. Res. 110, C02020. https://doi.org/10.1029/2003JC002258.

Phillips, O., 1958. The equilibrium range in the spectrum of wind-generated waves. J. Fluid Mech. 4, 426–433. https://doi.org/10.1017/S0022112058000550.

Phillips, O., 1985. Spectral and statistical properties of the equilibrium range in wind-generated gravity waves. J. Fluid Mech. 156, 505–531. https://doi.org/10.1017/S0022112085002221.

Pierson, W., Moskowitz, L., 1964. A proposed spectral form for fully developed wind-seas based on the similarity theory of S.A. Kitaigorodskii. J. Geophys. Res. 69, 5181–5190. https://doi.org/10.1029/JZ069i024p05181.

Plant, W., 1982. A relationship between wind stress and wave slope. J. Geophys. Res. 87, 1961–1967. https://doi.org/10.1029/JC087iC03p01961.

Potter, H., 2015. Swell and the drag coefficient. Ocean Dyn. 65 (3), 375–384. https://doi.org/10.1007/s10236-015-0811-4.

Pushkarev, A., Resio, D., Zakharov, V., 2003. Weak turbulent approach to the wind-generated gravity sea waves. Physica D 184, 29–63. https://doi.org/10.1016/S0167-2789(03)00212-4.

Resio, D., Long, C., Vincent, C., 2004. Equilibrium-range constant in wind-generated wave spectra. J. Geophys. Res. 109 (C1). https://doi.org/10.1029/2003JC001788.

Resio, D., Swail, V., Jensen, R., Vardone, V., 1999. Wind speed scaling in fully developed seas. J. Phys. Oceanogr. 29, 1801–1811. https://doi.org/10.1175/1520-0485(1999)029<1801:WSSIFD>2.0.CO;2.

Rieder, K., Smith, J., 1998. Removing wave effects from the wind stress vector. JGR Oceans 103 (C1), 1363–1364. https://doi.org/10.1029/97JC02571.

Romero, L., Melville, W., 2010. Airborne observations of fetch-limited waves in the Gulf of Tehuantepec. J. Phys. Oceanogr. 40 (3), 441–465. https://doi.org/10.1175/2009JPO4127.1.

Erik Sahlée, E., Drennan, W., Henry Potter, H., Rebozo, M., 2012. Waves and air-sea fluxes from a drifting ASIS buoy during the southern ocean gas exchange experiment. JGR Oceans 117 (C080030). https://doi.org/10.1029/2012JC008032.

Semedo, A., Suselj, K., Rutgerson, A., Steel, A., 2011. A global view of wind-sea and swell climate from ERA-40. J. Clim. 24, 1462-'479. https://doi.org/10.1175/2010JCLI3718.1.

Smedman, A., Högstrom, U., Bergström, H., Rutgersson, A., Kahma, K., Pettersson, H., 1999. A case study of air-sea interaction during swell conditions. JGR Oceans 104 (C11), 25831–25833. https://doi.org/10.1029/1999JC900213.

Smedman, A., Högström, U., Sahleé, E., 2009a. Observational study of marine atmospheric boundary layer characteristics during swell. J. Atmos. Sci. 66, 2747–2764. https://doi.org/10.1175/2009JAS2952.1.

Smedman, A., Högström, U., Sahleé, E., Drennan, W., Kahma, K., Pettersson, H., Zhang, F., 2009b. The atmospheric boundary layer during swell: a field study and interpretation of the turbulent kinetic energy budget for high wave ages. J. Atmos. Sci. 66, 2764–2779. https://doi.org/10.1175/2009JAS2973.1.

Smedman, A., Larsen, X., Högstrom, U., Kahma, K., Pettersson, H., 2003. Effect of sea state on the Momentum exchange over the sea during neutral conditions. JGR Oceans 108 (C11). https://doi.org/10.1029/2002JC001526.

Smith, S.D., 1980. Wind Stress and heat flux over the ocean in gale force winds. J. Phys. Oceanogr. 10, 709–726. https://doi.org/10.1175/1520-0485(1980)010<0709:WSAHFO>2.0.CO;2.

Snodgrass, F., Groves, G., Hasselmann, K., Miller, G., Munk, W., Powers, W., 1966. Propagation of ocean swell across the Pacific. Philos. Trans. R. Soc. London, Ser. A 249, 431–497. https://doi.org/10.1098/rsta.1966.0022.

Sullivan, P., Edson, J., Hristov, T., McWilliams, J., 2008. Large-eddy simulations and observations of atmospheric marine boundary layers above nonequilibrium surface waves. J. Atmos. Sci. 65, 1225–1240. https://doi.org/10.1175/2007JAS2427.1.

Tamura, H., Waseda, T., Miyazawa, Y., 2009. Freakish sea state and swell-wind-sea coupling: Numerical study of the Suwa-Maru incident. Geophys. Res. Lett. 36, L01607. https://doi.org/10.1029/2008GL036280.

Tamura, H., Drennan, W., Sahlee, E., Graber, H.C., 2014. Spectral form and source term balance of short gravity wind waves. J. Geophys. Res. Oceans 119 (11), 7406–7419. https://doi.org/10.1002/2014JC009869.

Tamura, H., Drennan, W., Collins III, C., Graber, H., 2018. Turbulent air flow and wave induced stress over the ocean. Boundary Layer Meteorol. https://doi.org/10.1007/

s10546-018-0359-1.
Tang, Dajun, Moum, James, Lynch, James, Abbot, Phil, Chapman, Ross, Dahl, Peter, Duda, Timothy, Gawarkiewicz, Glen, Glenn, Scott, Goff, John, Graber, Hans, Kemp, John, Maffei, Andrew, Nash, Jonathan, Newhall, Arthur, 2007. Shallow water '06: A joint acoustic propagation/nonlinear internal wave physics experiment. Oceanog. 20 (4), 156–167 Special Issue on Ocean Exploration.
Thomson, J., D'Asaro, E., Cronin, M., Rogers, W., Harcourt, R., Shcherbina, A., 2013. Waves and the equilibrium range at Ocean Weather Station P. J. Geophys. Res. 118, 5951–5962. https://doi.org/10.1002/2013JC008837.
Toba, Y., 1973. Local balance in the air-sea boundary process. J. Oceanographic Soc. Japan 29, 209–220. https://doi.org/10.1007/BF02108528.
Tolman, H., Chalikov, D., 1996. Source terms in a third-generation wind-wave model. J. Phys. Oceanogr. 26, 2497–2518. https://doi.org/10.1175/1520-0485(1996)026<2497:STIATG>2.0.CO;2.
Tolman, H., WAVEWATCH III ® Development Group, 2014. User Manual and System Documentation of WAVEWATCH III® version 4.18. Technical Note 316, NOAA/NWS/NCEP/MMAB, 282 pp. + Appendices.
WAMDI Group, (13 authors), 1988. The WAM model- a third generation ocean wave prediction model. J. Phys. Oceanography, 18, 1775–1810, https://doi.org/10.1175/1520-0485(1988)018<1775:TWMTGO>2.0.CO;2.
Wu, J., 1982. Wind-stress coefficients over sea surface from breeze to hurricane. J. Geophys. Res. 87, 9704–9706. https://doi.org/10.1029/JC087iC12p09704.
Young, I., Babanin, A., Zeigler, S., 2013. The decay rate of ocean swell observed by altimetry. J. Phys. Oceanogr. 43, 2322–2333. https://doi.org/10.1175/JPO-D-13-083.1.